

## Electronic Supplementary Information

### **An ultralight charged MOF as fluoro-switchable monitor for assorted organo-toxins: size-exclusive dye scrubbing and anticounterfeiting applications *via* Tb<sup>3+</sup> sensitization**

Nilanjan Seal,<sup>a,b</sup> Ranadip Goswami,<sup>a,b</sup> Manpreet Singh,<sup>a,b</sup> Renjith S. Pillai,<sup>\*,c</sup> and Subhadip Neogi<sup>\*,a,b</sup>

<sup>a</sup>Academy of Scientific and Innovative Research (AcSIR), Ghaziabad-201002, India

<sup>b</sup>Inorganic Materials & Catalysis Division, CSIR-Central Salt & Marine Chemicals Research Institute, Bhavnagar, Gujarat 364002, India

<sup>c</sup>Department of Chemistry, Faculty of Engineering and Technology, SRM Institute of Science and Technology, Kattankulathur 603203, Chennai, Tamil Nadu, India

\*E-mail: [renjiths@srmist.edu.in](mailto:renjiths@srmist.edu.in)

\*E-mail: [sneogi@csmcri.res.in](mailto:sneogi@csmcri.res.in)

### Table of contents

1.	Materials and Physical measurements	Page S-3
2.	Single Crystal X-ray Crystallography	Page S-3
3.	Experimental section	Page S-4
4.	Fig. S1. Optical microscopic image of <b>CSMCRI-4</b> .	Page S-5
5.	Fig. S2. (a) View of the anionic [Li <sub>2</sub> (COO) <sub>4</sub> ] <sup>2-</sup> SBU. (b) Different coordination modes of TCA ligand in <b>CSMCRI-4</b> . (c) Topological representation of <b>CSMCRI-4</b> along <i>c</i> direction. (d) Topological representation along <i>b</i> direction.	Page S-5
6.	Fig. S3. Thermogravimetric analysis of as-synthesized <b>CSMCRI-4</b> .	Page S-6
7.	Fig. S4. (a) FT-IR spectra (KBr pellet, cm <sup>-1</sup> ) of <b>CSMCRI-4</b> . (b) N <sub>2</sub> adsorption isotherm of <b>4a</b> at 77 K (inset shows pore-size distribution plot).	Page S-6
8.	Fig. S5. (a) Simulated and as-synthesized powder X-ray diffraction (PXRD) patterns for <b>CSMCRI-4</b> . (b) PXRD pattern of as-synthesized <b>CSMCRI-4</b> after activation and after immersing in water for 6 hours.	Page S-7
9.	Fig. S6. UV-Vis spectra of H <sub>3</sub> TCA and <b>4a</b> .	Page S-7
10.	Fig. S7. Emission intensity of <b>4a</b> dispersed in various solvents.	Page S-8
11.	Fig. S8. Emission intensity of H <sub>3</sub> TCA and <b>4a</b> (dispersed in DMF).	Page S-8
12.	Fig. S9. Fluorescence quenching efficiency of <b>4a</b> (1 mg/ 2 mL DMF) for studied pesticides.	Page S-9
13.	Fig. S10. Emission spectra of <b>4a</b> upon incremental addition of other pesticide solutions (2 mM, 200 μL).	Page S-9
14.	Fig. S11. The curvature of the S-V plot for 2 mM dichloran (DCNA) solution (0 to 200 μL).	Page S-10
15.	Fig. S12. Stern-Volmer (S-V) plot for 2 mM DCNA solution (0 to 200 μL).	Page S-10
16.	Fig. S13. Linear region of fluorescence intensity of <b>4a</b> upon addition of DCNA (0 – 200 μL, 10 μM stock solution).	Page S-11
17.	Fig. S14. Reproducibility of quenching efficiency of <b>4a</b> towards 2 mM DCNA solution up to five sensing-recovery cycles.	Page S-11
18.	Fig. S15. PXRD patterns of <b>4a</b> obtained after five sensing-recovery cycles for DCNA (2 mM).	Page S-12

19.	Fig. S16. HOMO–LUMO energies for MOF ( <b>4a</b> ) along with the studied pesticide molecules.	Page S-12
20.	Fig. S17. Fluorescence quenching efficiency of <b>4a</b> (1 mg/ 2 mL DMF) towards studied antibiotics.	Page S-13
21.	Fig. S18. Emission spectra of <b>4a</b> upon incremental addition of other antibiotic solution (1 mM, 200 $\mu$ L).	Page S-13 to S-14
22.	Fig. S19. The curvature of the S–V plot for 1 mM NZF solution (0 to 200 $\mu$ L).	Page S-15
23.	Fig. S20. Stern-Volmer (S-V) plot for 1 mM NZF solution (0 to 200 $\mu$ L).	Page S-15
24.	Fig. S21. Linear region of fluorescence intensity of <b>4a</b> upon addition of NZF (0 – 200 $\mu$ L, 10 $\mu$ M stock solution).	Page S-16
25.	Fig. S22. Reproducibility of quenching efficiency of <b>4a</b> towards 1 mM NZF solution up to five sensing-recovery cycles.	Page S-16
26.	Fig. S23. PXRD patterns of <b>4a</b> obtained after five sensing-recovery cycles for NZF (1 mM).	Page S-17
27.	Fig. S24. HOMO–LUMO energies for MOF ( <b>4a</b> ) along with the studied antibiotic molecules.	Page S-17
28.	Fig. S25. The single unit cell (1 $\times$ 1 $\times$ 1 simulation box) considered for the DFT calculations viewed along <i>c</i> for <b>4a</b> .	Page S-18
29.	Fig. S26. (a) The supper cells (2 $\times$ 1 $\times$ 2) DFT optimized <b>4a</b> viewed along <i>c</i> direction with slight tilting to view properly and (b) the super cells exposing the [101] miller plane (solid green planes) of DFT optimized <b>4a</b> . The slab cut exposing the [101] miller plane (solid green lines) of <b>4a</b> , showing the different orientations (c) along <i>c</i> and (d) along <i>a</i> .	Page S-19
30.	Fig. S27. (a), (b) and (c) DFT-optimized <b>4a</b> [101] surface, DCNA@ <b>4a</b> [101] surface and NZF@ <b>4a</b> [101] surface viewed along <i>c</i> direction. (d), (e) and (f) DFT-optimized <b>4a</b> [101] surface, DCNA@ <b>4a</b> [101] surface and NZF@ <b>4a</b> [101] surface viewed along <i>a</i> direction.	Page S-20
31.	Fig. S28 to S29. DFT optimized structures of pesticide and antibiotic molecules.	Page S-21 to S-22
32.	Fig. S30. Emission spectra of Ln <sup>3+</sup> @ <b>4a</b> (Ln = La, Ce, Gd, Nd and Eu).	Page S-23
33.	Fig. S31. The EDX pattern of Tb <sup>3+</sup> @ <b>4a</b> .	Page S-23
34.	Fig. S32. Elemental mapping patterns of Tb <sup>3+</sup> @ <b>4a</b> (a) Terbium, (b) Nitrogen, (c) Carbon and (d) oxygen.	Page S-24
35.	Fig. S33. PXRD patterns of <b>4a</b> obtained after immersing in terbium nitrate solution (10 mM).	Page S-24
36.	Fig. S34. Emission spectra of Tb <sup>3+</sup> @ <b>4a</b> after addition of Na <sub>2</sub> EDTA and NH <sub>4</sub> F.	Page S-25
37.	Fig. S35. UV-vis spectra of methyl orange, congo red, Bismarck brown and thymol blue solutions in DMF (10 ppm), respectively, in presence of <b>4a</b> monitored at different time intervals.	Page S-25
38.	Fig. S36. UV-vis spectra of mixed MB <sup>+</sup> /TB <sup>0</sup> solution in DMF in presence of <b>4a</b> monitored at different time intervals.	Page S-26
39.	Fig. S37. Concentration changes of crystal violet (CV <sup>+</sup> ) solution with time.	Page S-26
40.	Fig. S38. DFT-optimized <b>4a</b> with MB <sup>+</sup> viewed along <i>c</i> .	Page S-27
41.	Fig. S39. DFT optimized structures of organic dye molecules.	Page S-27 to S-28
42.	Fig. S40. Emission spectra of <b>4a</b> (black) and MB <sup>+</sup> @ <b>4a</b> (red).	Page S-28
43.	Fig. S41. PXRD patterns of <b>4a</b> obtained after methylene blue adsorption.	Page S-28
44.	Fig. S42. FE-SEM images of (a) pristine <b>4a</b> and (b) <b>4a</b> after exchange with methylene blue.	Page S-29
45.	Fig. S43. UV-vis spectra of MB <sup>+</sup> release from MB <sup>+</sup> @ <b>4a</b> in pure DMF.	Page S-29
46.	Fig. S44. PXRD patterns of <b>4a</b> obtained after methylene blue release.	Page S-30

47.	Table S1. Crystallographic data and refinement parameters for <b>CSMCRI-4</b> .	Page S-30
48.	Table S2. Calculation of standard deviation of fluorescence intensity and limit of detection for <b>4a</b> towards dichloran (DCNA).	Page S-31
49.	Table S3. Calculation of standard deviation of fluorescence intensity and limit of detection for <b>4a</b> towards NZF.	Page S-31
50.	Table S4. A comparison of quenching constant, their LOD values, of various luminescent MOFs used for detection of DCNA.	Page S-32
51.	Table S5. A comparison of quenching constant, their LOD values, of various luminescent MOFs used for detection of NZF.	Page S-32
52.	Table S6. HOMO and LUMO energy levels of different pesticides calculated by density functional theory (DFT) using CP2K package.	Page S-33
53.	Table S7. HOMO and LUMO energy levels of different antibiotics calculated by density functional theory (DFT) using CP2K package.	Page S-33
54.	Table S8. HOMO and LUMO energy levels of <b>4a</b> , DCNA@ <b>4a</b> and NZF@ <b>4a</b> calculated by density functional theory (DFT) using CP2K package.	Page S-33
55.	Table S9. Cell parameters of <b>4a</b> obtained by DFT optimization.	Page S-33
56.	Table S10. Determination of solvent composition and molecular formula of <b>CSMCRI-4</b> .	Page S-34
57.	Table S11. ICP-OES results for Tb <sup>3+</sup> @ <b>4a</b> .	Page S-34
58.	Table S12. Selective adsorption of methylene blue in different organic solvents by recent MOFs.	Page S-35

## Materials and Physical measurements

All the solvents and reagents were purchased from commercial sources (except H<sub>3</sub>TCA) and used without further purification. Thermogravimetric analyses (TGA) (heating rate of 10 °C/min under N<sub>2</sub> atmosphere) were performed with a Mettler Toledo Star SW 8.10 system. The Fourier Transform infrared-spectra (FT-IR) of the samples were recorded using the KBr pellet method on a Perkin–Elmer GX FTIR spectrometer in the region of 400–4000 cm<sup>-1</sup>. Nitrogen adsorption, BET surface area and NLDFT porosity measurements were conducted at 77 K on a Quantachrome Autosorb IQ instrument. Powder X-ray diffraction (PXRD) data were collected using a PANalytical Empyrean (PIXcel 3D detector) system equipped with Cu K $\alpha$  ( $\lambda=1.54$  Å) radiation. Microanalyses of the compounds were conducted using elementarvario MICRO CUBE analyzer. UV-Vis spectra recorded using Shimadzu UV-3101 PC spectrometer and the luminescence experiments were performed at room temperature using a Fluorolog Horiba JobinYvon spectrophotometer.

## Single Crystal X-ray Crystallography

Single crystals with suitable dimensions were chosen under an optical microscope and mounted on a glass fibre for data collection. Intensity data for as-synthesized light yellow crystal of **CSMCRI-4** were collected using graphite-monochromated MoK $\alpha$  ( $\lambda=0.71073$  Å) radiation on a Bruker SMART APEX diffractometer equipped with CCD area detector at 173 K, The linear absorption coefficients, scattering factors for the atoms, and the anomalous dispersion corrections were taken from International Tables for X-ray Crystallography. The data integration and reduction were performed with SAINT<sup>1</sup> software. Absorption corrections to the collected reflections were accounted with SADABS<sup>2</sup> using XPREP.<sup>3</sup> The structure was solved by direct method using SIR-97<sup>4</sup> and was refined on  $F^2$  by the full-matrix least-squares technique using the SHELXL-2014<sup>5</sup> program package. All H atoms were placed in calculated positions using idealized geometries (riding model) and assigned fixed isotropic displacement parameters using the SHELXL default. To give an account of disordered electron

densities associated with solvent molecules, the "SQUEEZE" protocol in PLATON<sup>6</sup> was applied that produced a set of solvent free diffraction intensities. Final cycles of least-squares refinements improved both the R values and Goodness of Fit with the modified data set after subtracting the contribution from the disordered solvent molecules, using SQUEEZE program. The crystal and refinement data for **CSMCRI-4** is listed in Table S1. Topological analysis was performed by using TOPOS software.<sup>7</sup>

## Experimental section

### Synthesis and characterization of the ligand

The ligand 4,4',4''-tricarboxytriphenylamine (H<sub>3</sub>TCA) was prepared by following a literature method<sup>8</sup>.

### Synthesis of CSMCRI-4

A mixture of LiNO<sub>3</sub> (30 mg, 0.43 mmol) and H<sub>3</sub>TCA (22 mg, 0.058 mmol) was dissolved in 4 mL of N,N-dimethylformamide (DMF) in a 15 mL screw-capped vial by ultrasonic treatment for 5 min. Then it was heated to 120 °C for 3 days, and then slowly cooled down to room temperature. The light yellow colored, X-ray quality crystals were obtained. The crystals were filtered, thoroughly washed with DMF and dried under vacuum (yield: 60%). Anal. Calcd. For [(CH<sub>3</sub>)<sub>2</sub>NH<sub>2</sub>]<sub>2</sub>[Li(TCA)]·0.5DMF·H<sub>2</sub>O: C, 59.57; H, 6.61; N, 9.92. Found: C, 59.71; H, 6.53; N, 10.02.

### Preparation of Lanthanide-doped Sample

Typically, 10 mg of finely ground **4a** was immersed in 2 mL DMF solution of Ln(NO<sub>3</sub>)<sub>3</sub>·6H<sub>2</sub>O (10 mM) (Ln<sup>3+</sup> = La<sup>3+</sup>, Ce<sup>3+</sup>, Gd<sup>3+</sup>, Nd<sup>3+</sup>, Tb<sup>3+</sup> and Eu<sup>3+</sup>). After soakage of 24 hours, the materials were washed several times with DMF and then dried under vacuum to obtain lanthanide encapsulated material (Ln<sup>3+</sup>@**4a**). After that dispersions were prepared with this dried material.

### Fluorescence Measurements

In a typical experimental procedure, 1 mg of finely ground **4a** was dispersed in 2 mL of fresh DMF to form a stable suspension after ultrasonic treatment for one hour. All fluorescence titration experiments were performed by gradually adding DMF solution of different analytes [pesticides (2 mM), and antibiotics (1 mM)]. Fluorescence detections were performed at the emission wavelength ranging from 360 to 550 nm with an excitation wavelength ( $\lambda_{ex}$ ) at 342 nm at room temperature. During the whole period of performing each titration, the dispersion was continuously stirred to maintain the uniformity. All titrations were conducted thrice, and consistent results were reported.

### Recyclable luminescence experiments

The reproducibility of **4a** towards sensing of DCNA and NZF was studied. After the first sensing experiment, the MOF powder was recovered by centrifugation and washed with DMF and chloroform several times. Subsequently, the material was vacuum dried and used for the next cycle of experiments.

### Dye adsorption and Separation

To evaluate the adsorption ability of **4a**, six dyes, namely, positively charged methylene Blue (MB<sup>+</sup>) and crystal violet (CV<sup>+</sup>); negatively charged methyl orange (MO<sup>-</sup>) and congo red (CR<sup>-</sup>); neutral dyes bismarck brown (BB<sup>0</sup>) and thymol blue (TB<sup>0</sup>) were selected. The activated samples (**4a**) (10 mg) were immersed into the DMF solution of these dyes (10 mL, 10 ppm) and the absorption measurements were carried out by UV-vis spectroscopy at predetermined time intervals. A similar method was also used to investigate the performance of dye separation; 10 mg of **4a** was immersed into 10 mL of mixed MB<sup>+</sup>& MO<sup>-</sup>, MB<sup>+</sup>& CR<sup>-</sup>, MB<sup>+</sup>& BB<sup>0</sup>, MB<sup>+</sup>& TB<sup>0</sup> and MB<sup>+</sup>& CV<sup>+</sup> dye solution.

### Measurement of Removal Efficiency

The extent of removal (%) of methylene blue at time t (min) was calculated using the following equation:

Removal efficiency (RE %) =  $(C_0 - C_t) / C_0$  where  $C_0$  (ppm) is the initial concentration of dye and  $C_t$  (ppm) is the concentration of dye in the solution at a specific time.

### Dye Release Experiment

Dye-releasing experiments were performed in pure DMF and saturated DMF solution of  $\text{NaNO}_3$ , respectively. UV-vis spectra were used to measure the release ability of **4a**.

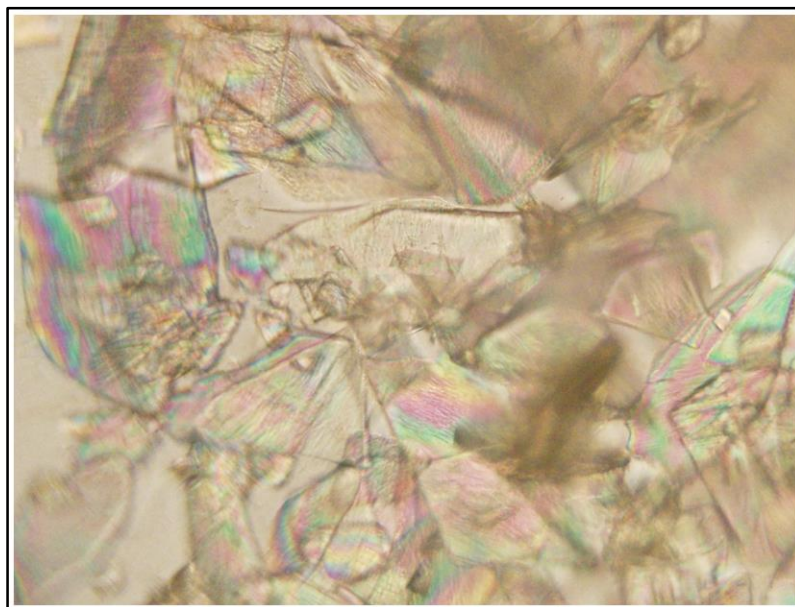


**Fig. S1.** Optical microscopic image of **CSMCRI-4**.

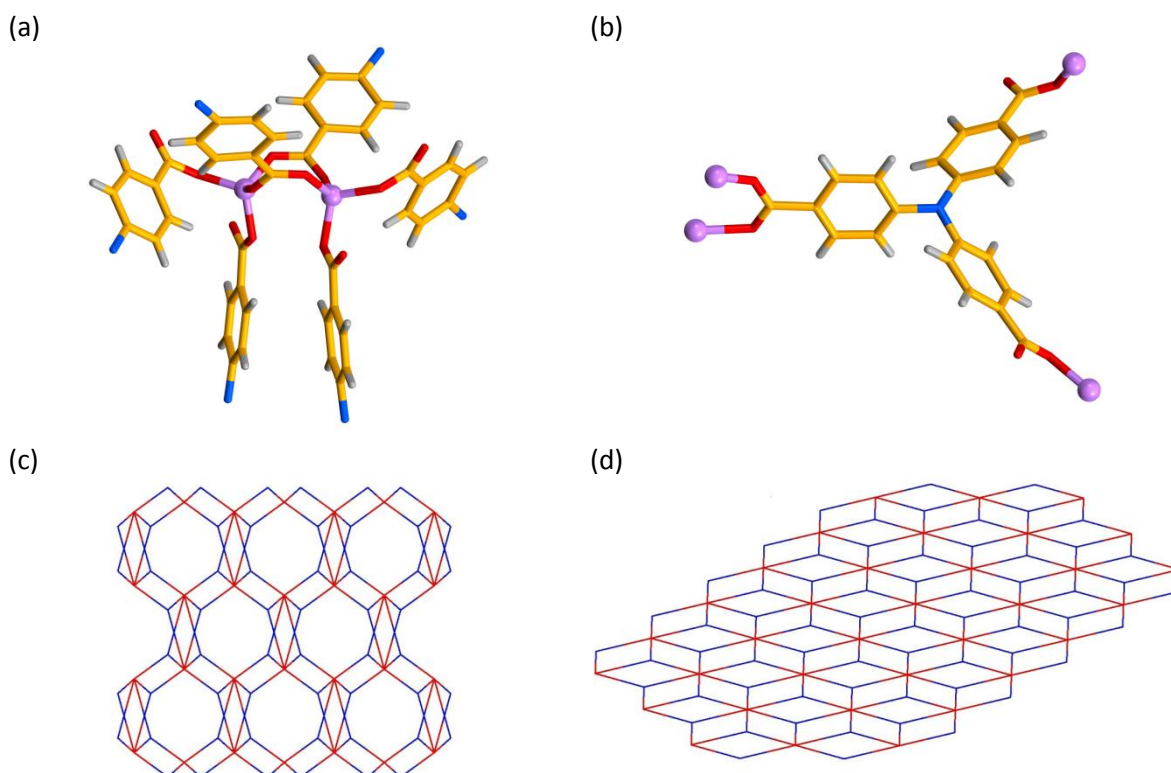


**Fig. S2.** (a) View of the anionic  $[\text{Li}_2(\text{COO})_4]^{2-}$  SBU. (b) Different coordination modes of TCA ligand in **CSMCRI-4**. (c) Topological representation of **CSMCRI-4** along *c* direction exhibiting a 3.6-connected anatase topology. (d) Topological representation along *b* direction.

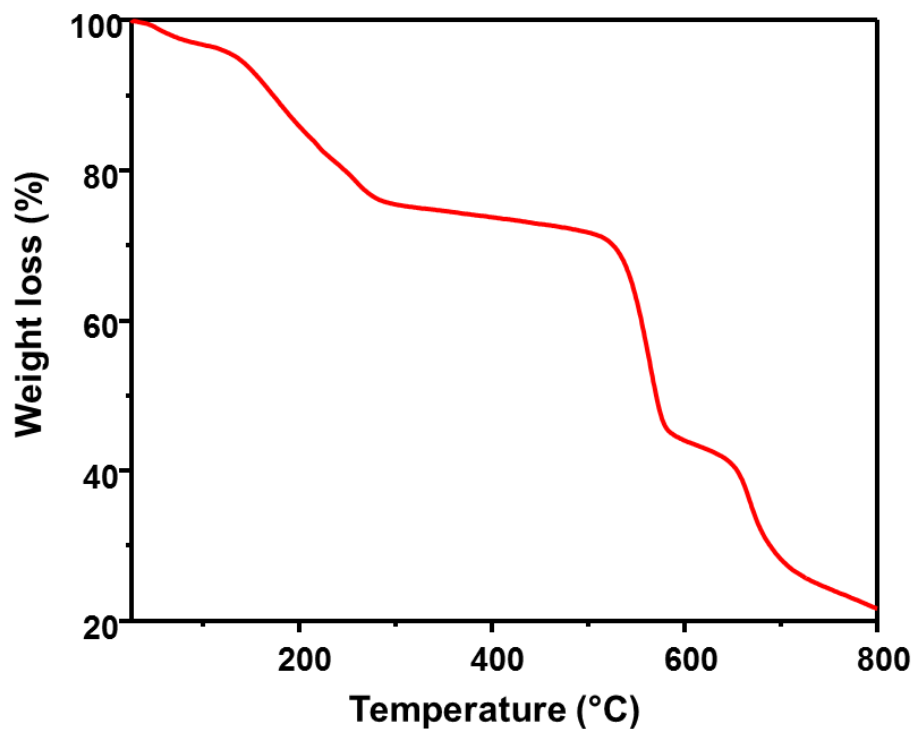


Fig. S3. Thermogravimetric analysis of as-synthesized CSMCRI-4.

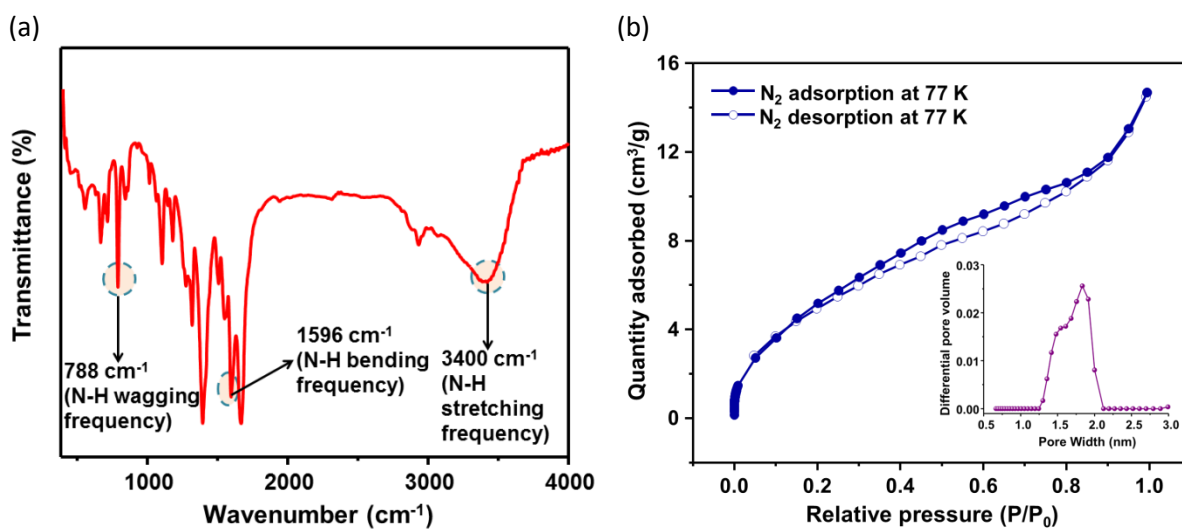
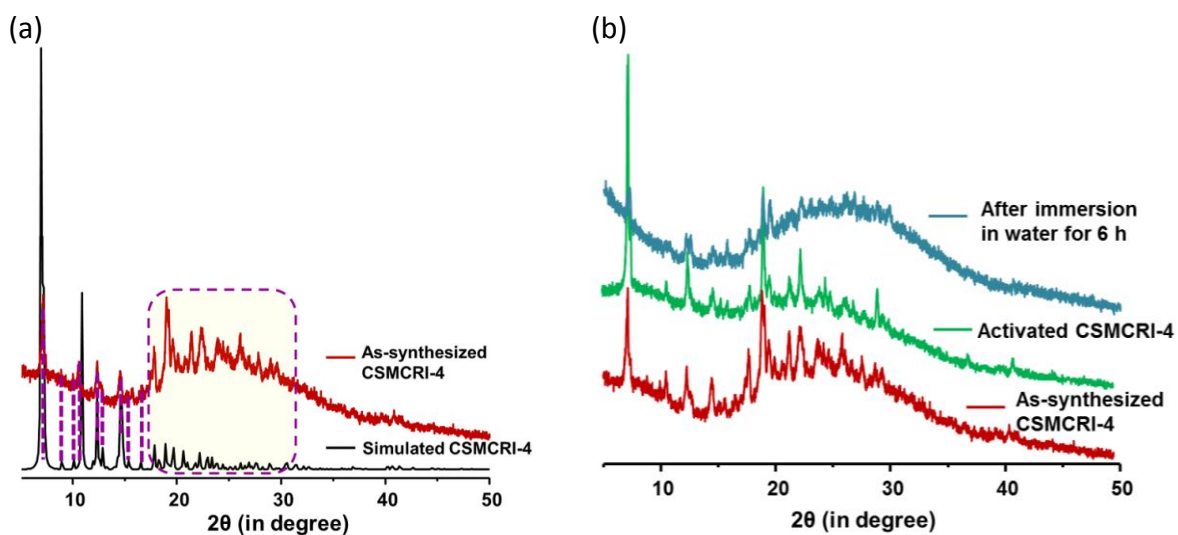
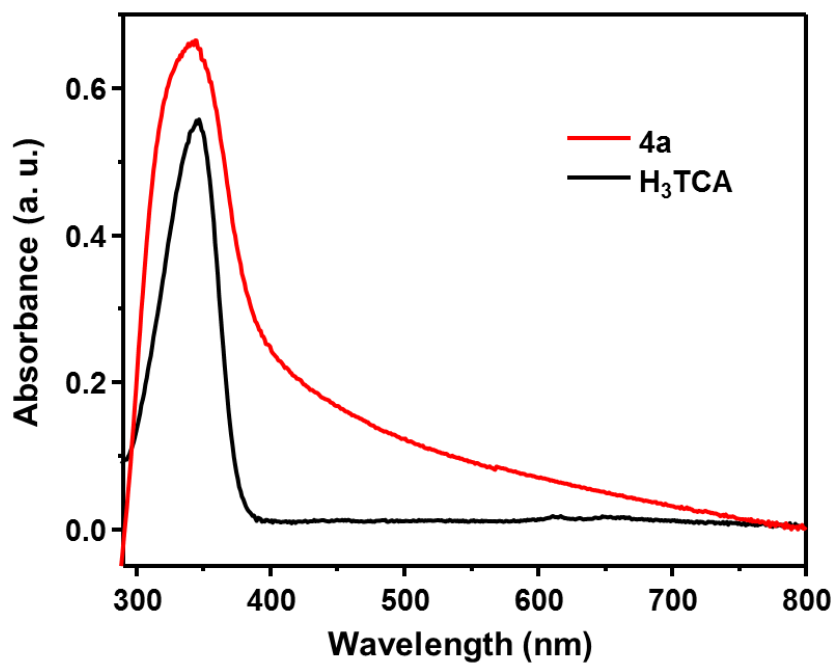


Fig. S4. (a) FT-IR spectra (KBr pellet,  $\text{cm}^{-1}$ ) of CSMCRI-4. (b)  $\text{N}_2$  adsorption isotherm of **4a** at 77 K (inset shows pore-size distribution plot).



**Fig. S5.** (a) Simulated and as-synthesized powder X-ray diffraction (PXRD) patterns for **CSMCRI-4** (peak to peak matching included). (b) PXRD pattern of as-synthesized **CSMCRI-4** after activation and after immersion in water for 6 hours.



**Fig. S6.** UV-Vis spectra of H<sub>3</sub>TCA and **4a** (dispersed in DMF).

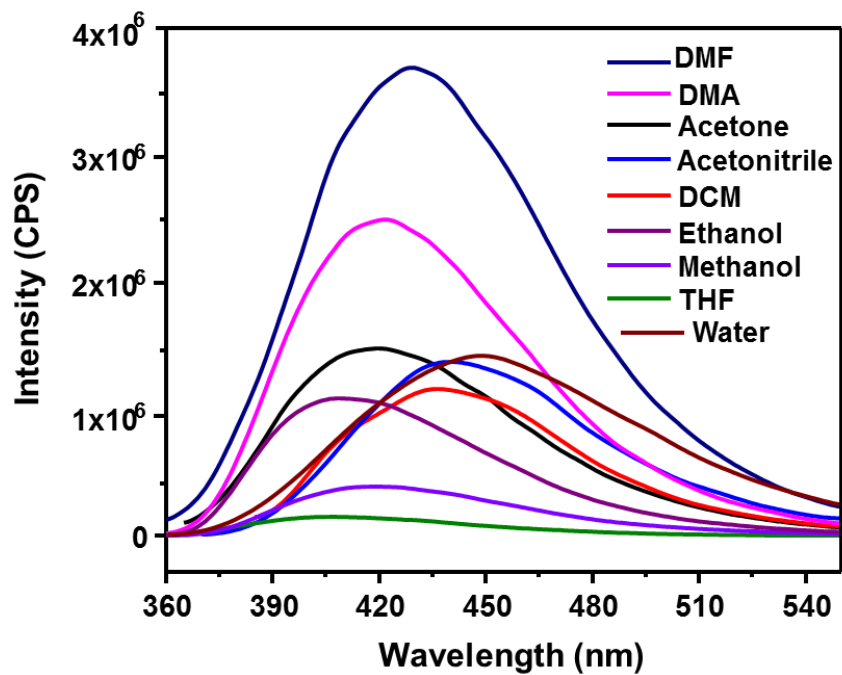


Fig. S7. Emission intensity of **4a** dispersed in various solvents.

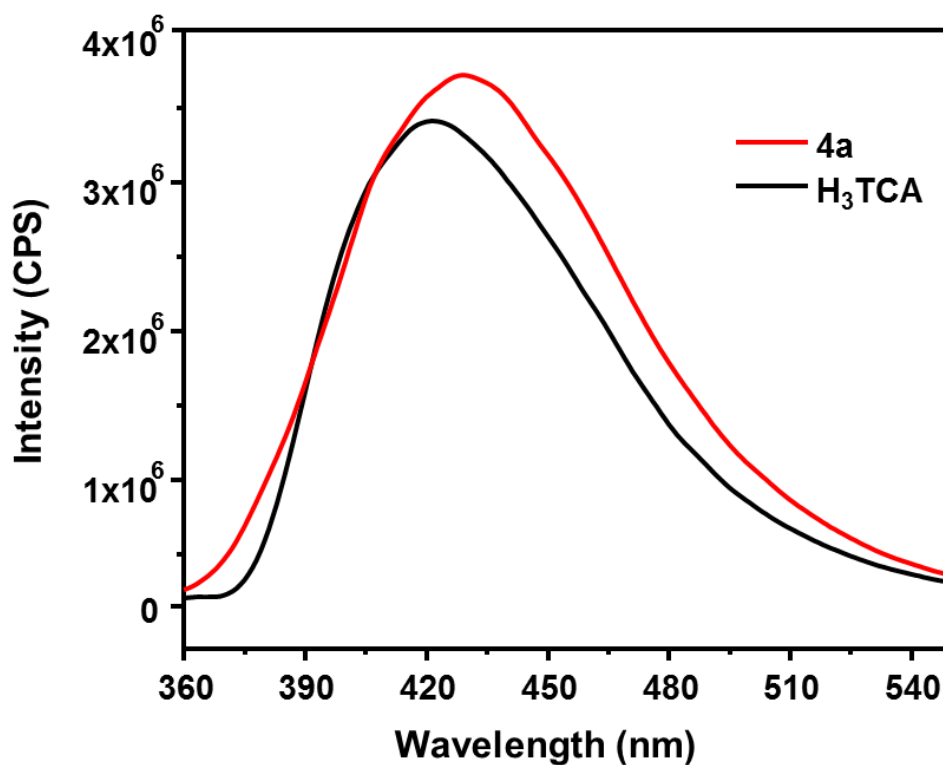
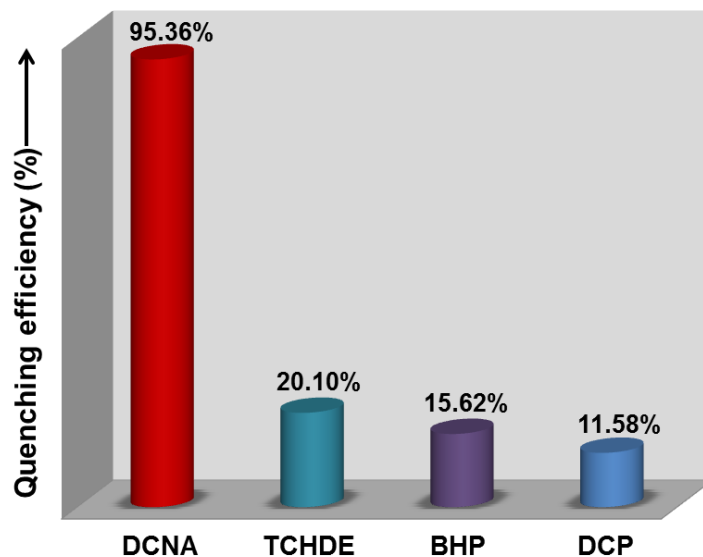
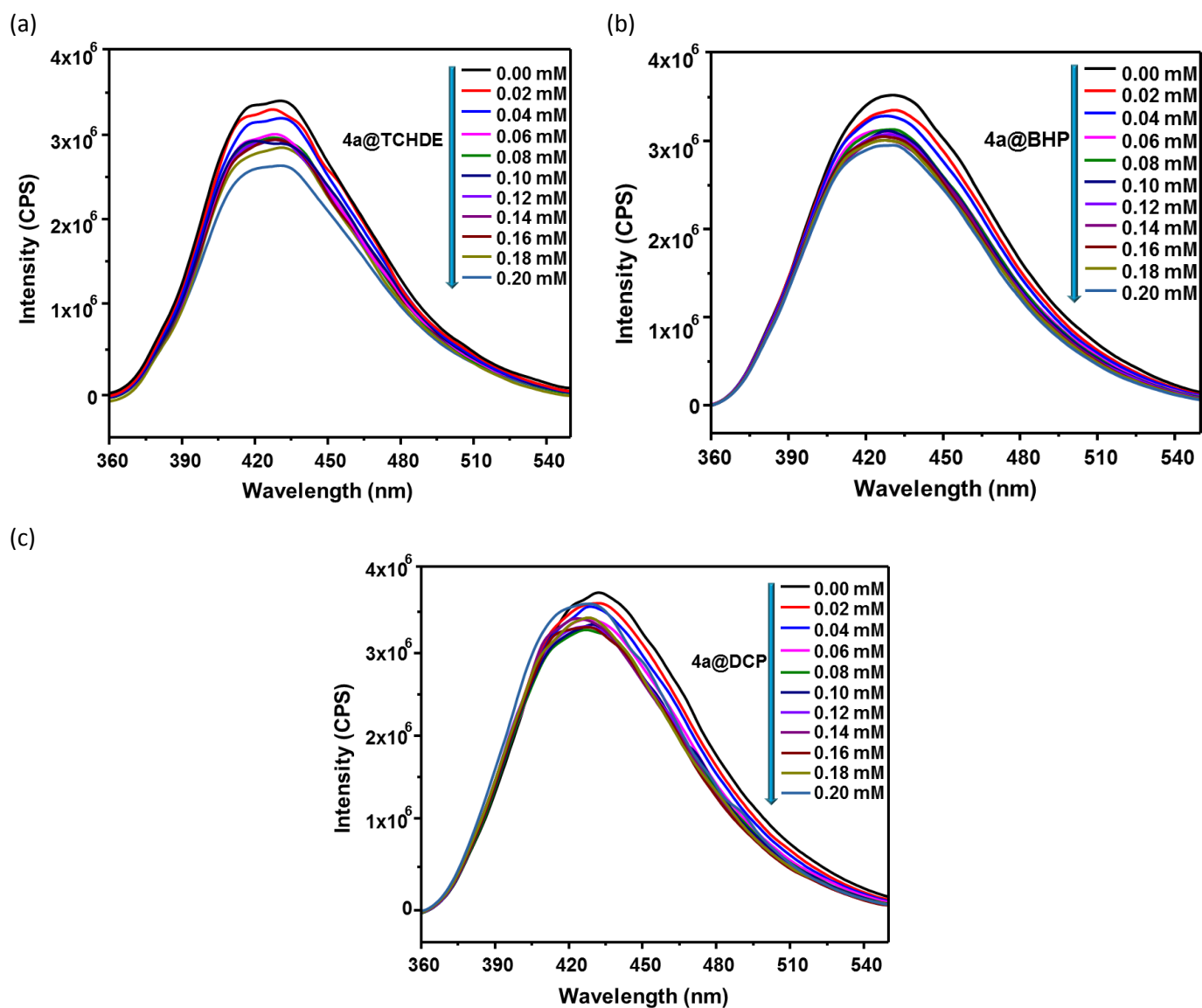


Fig. S8. Emission intensity of  $H_3TCA$  and **4a** (dispersed in DMF).



**Fig. S9.** Fluorescence quenching efficiency of **4a** (1 mg/ 2 mL DMF) for studied pesticides. Quenching efficiency of **4a** is calculated using equation  $(I_0 - I)/I_0 \times 100\%$ , where  $I_0$  and  $I$  denotes the emission intensities before and after the addition of studied analytes, respectively.



**Fig. S10.** Emission spectra of **4a** upon incremental addition of (a) 2,4,4'-Trichloro-2'-hydroxydiphenyl Ether (TCHDE) (b) 2,2-Bis(4-hydroxyphenyl) propane (BHP) and (c) 2,4-Dichlorophenol (DCP) solutions (each of 2 mM, 200  $\mu$ L).

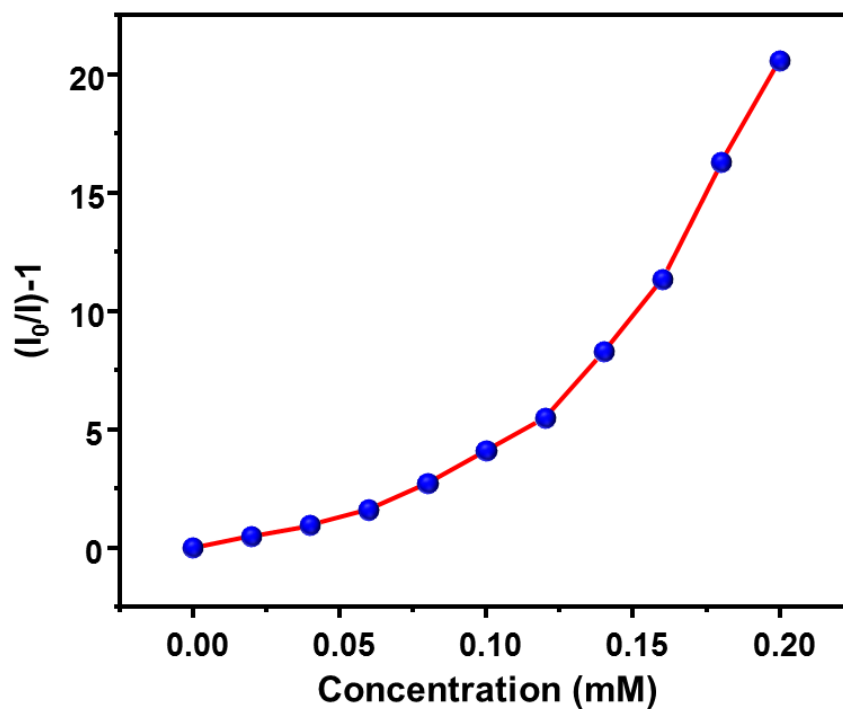


**Fig. S11.** The curvature of the S–V plot for 2 mM dichloran (DCNA) solution (0 to 200  $\mu$ L).

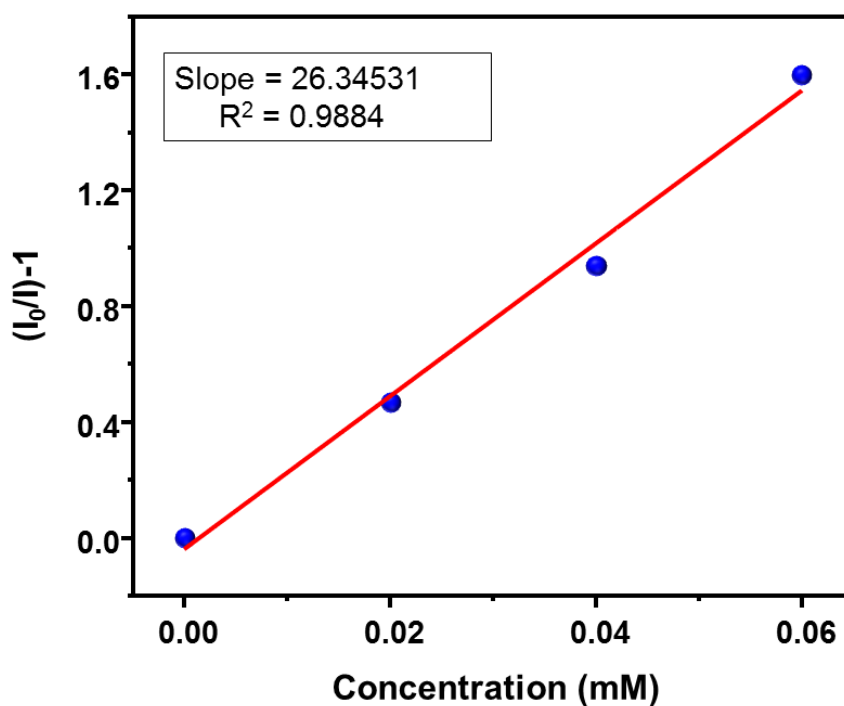


**Fig. S12.** Stern-Volmer (S-V) plot for 2 mM DCNA solution (0 to 200  $\mu$ L). The relative fluorescence intensity  $(I_0/I)-1$  is linear with DCNA concentration in the range of 0–0.06 mM.

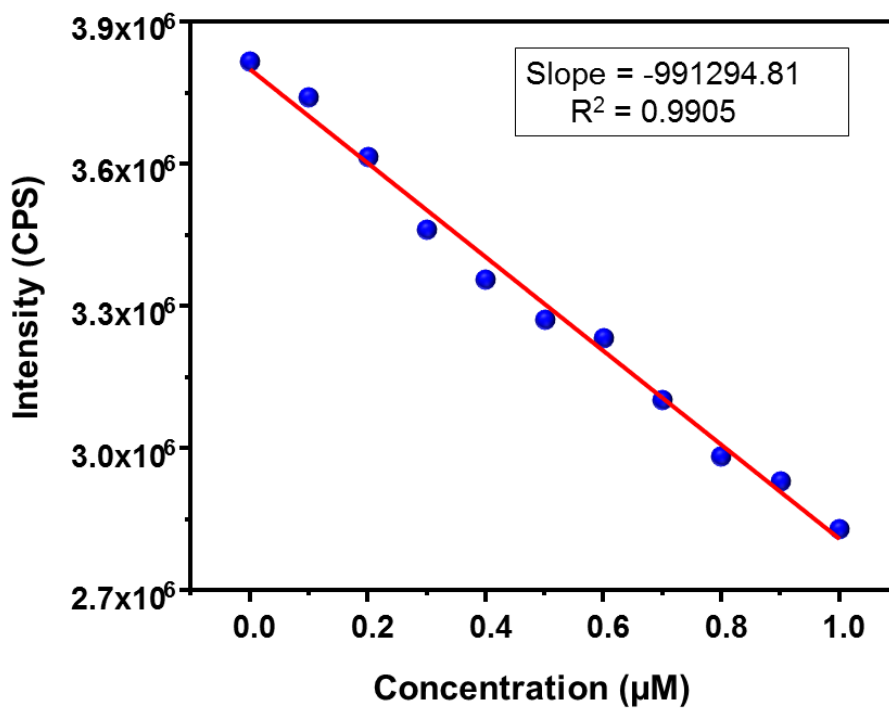


**Fig. S13.** Linear region of fluorescence intensity of **4a** upon addition of DCNA (0 to 200  $\mu\text{L}$ , 10  $\mu\text{M}$  stock solution).

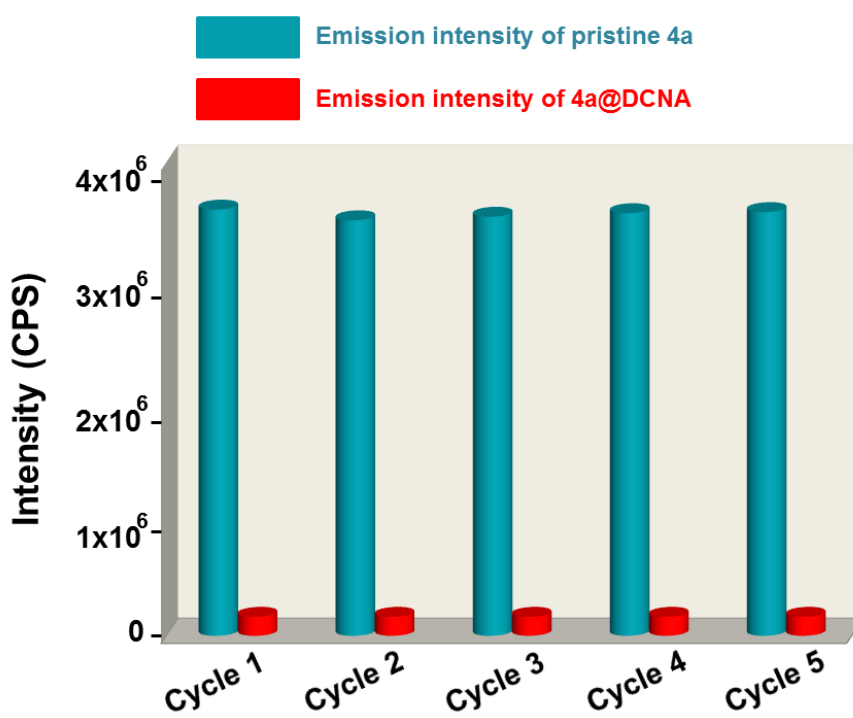


**Fig. S14.** Reproducibility of quenching efficiency of **4a** towards 2 mM DCNA solution up to five sensing-recovery cycles.

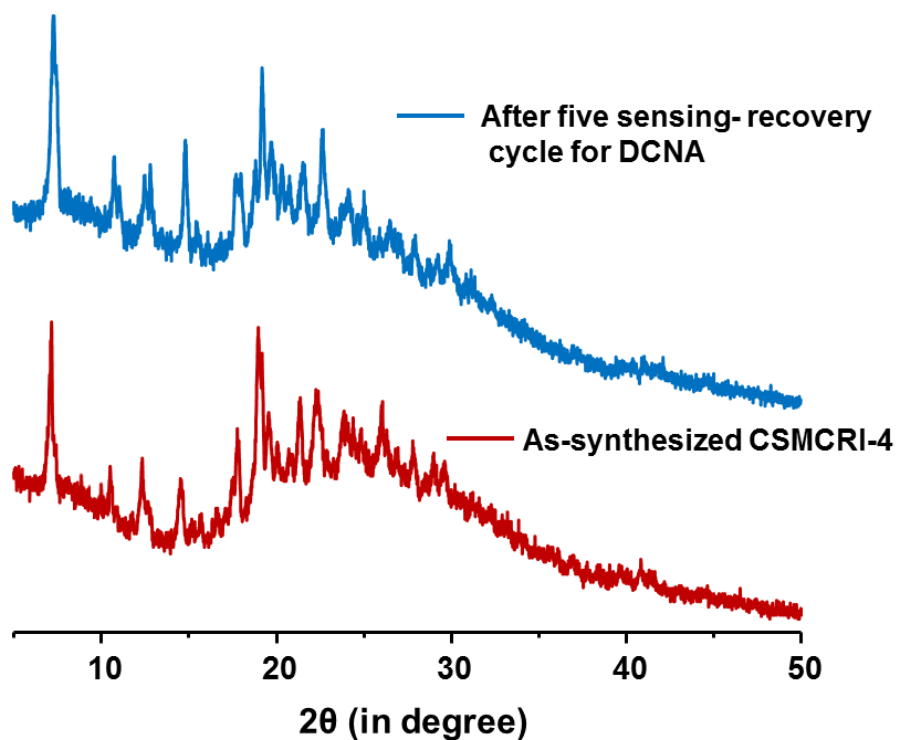


**Fig. S15.** PXRD patterns of **4a** obtained after five sensing-recovery cycles for DCNA (2 mM), revealing that structural integrity of the framework is maintained.

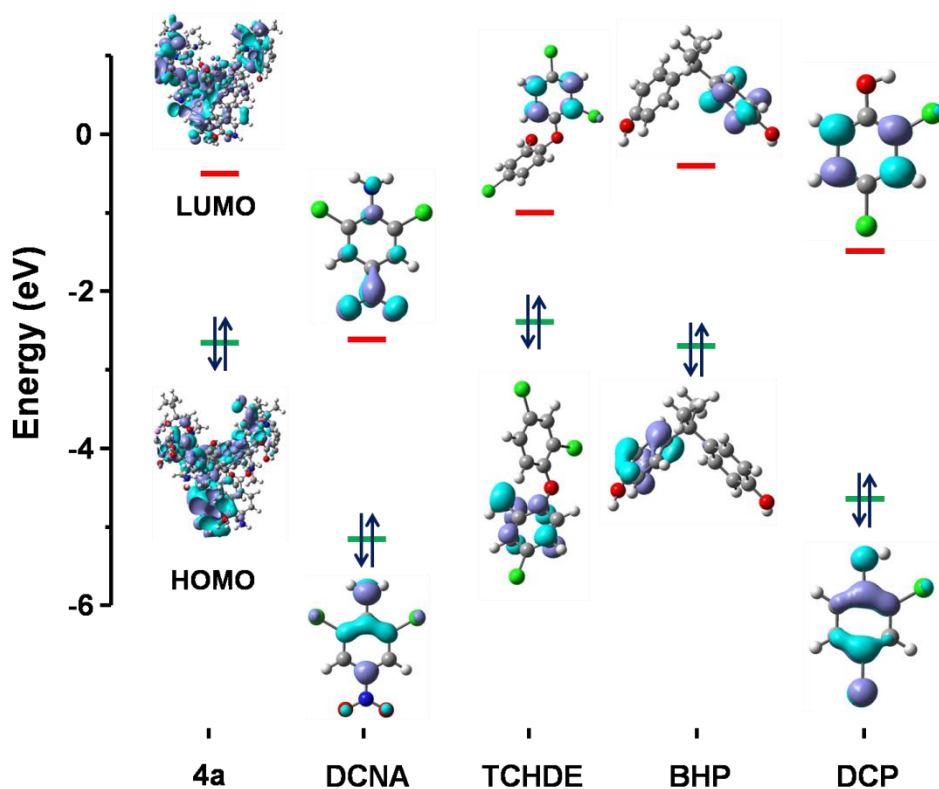


**Fig. S16.** HOMO–LUMO energies for MOF (**4a**) along with the studied pesticide molecules.

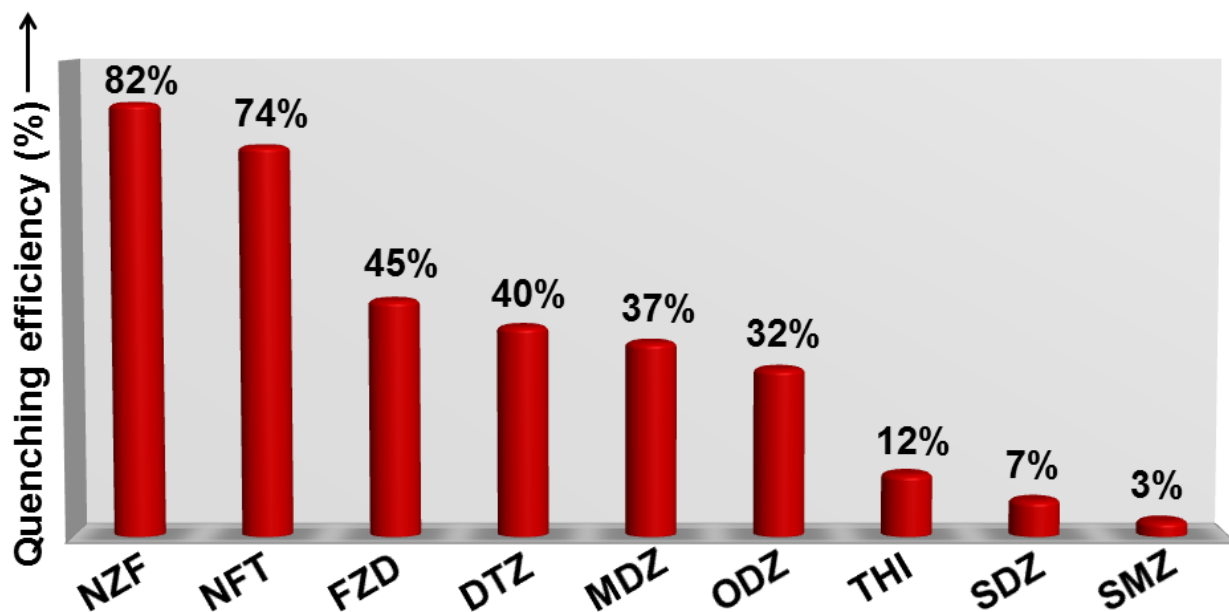
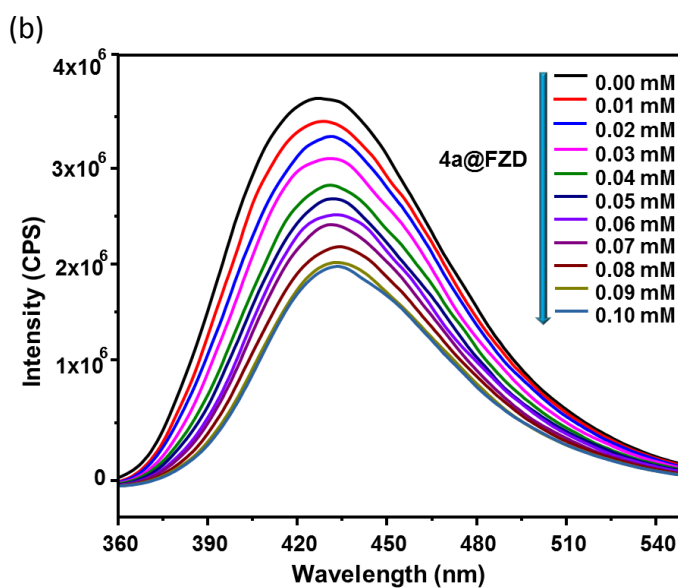
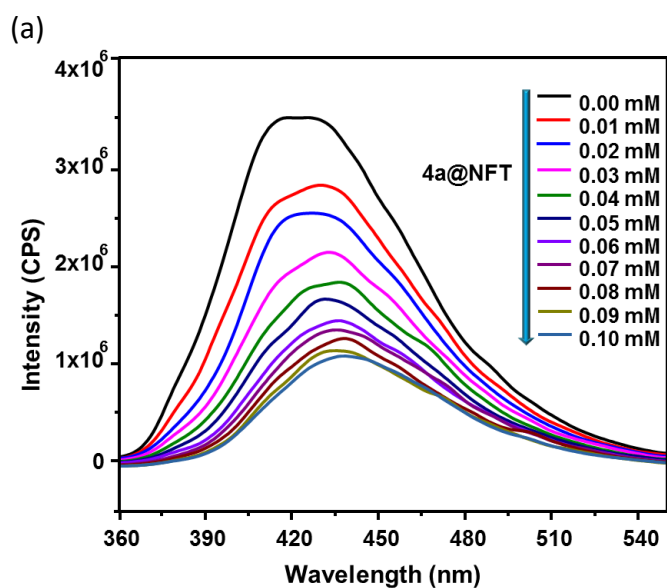


**Fig. S17.** Fluorescence quenching efficiency of **4a** (1 mg/ 2 mL DMF) towards studied antibiotics. Quenching efficiency of **4a** is calculated using equation  $(I_0 - I)/I_0 \times 100\%$ , where  $I_0$  and  $I$  denotes the emission intensities before and after the addition of studied analytes, respectively.



(c)

(d)

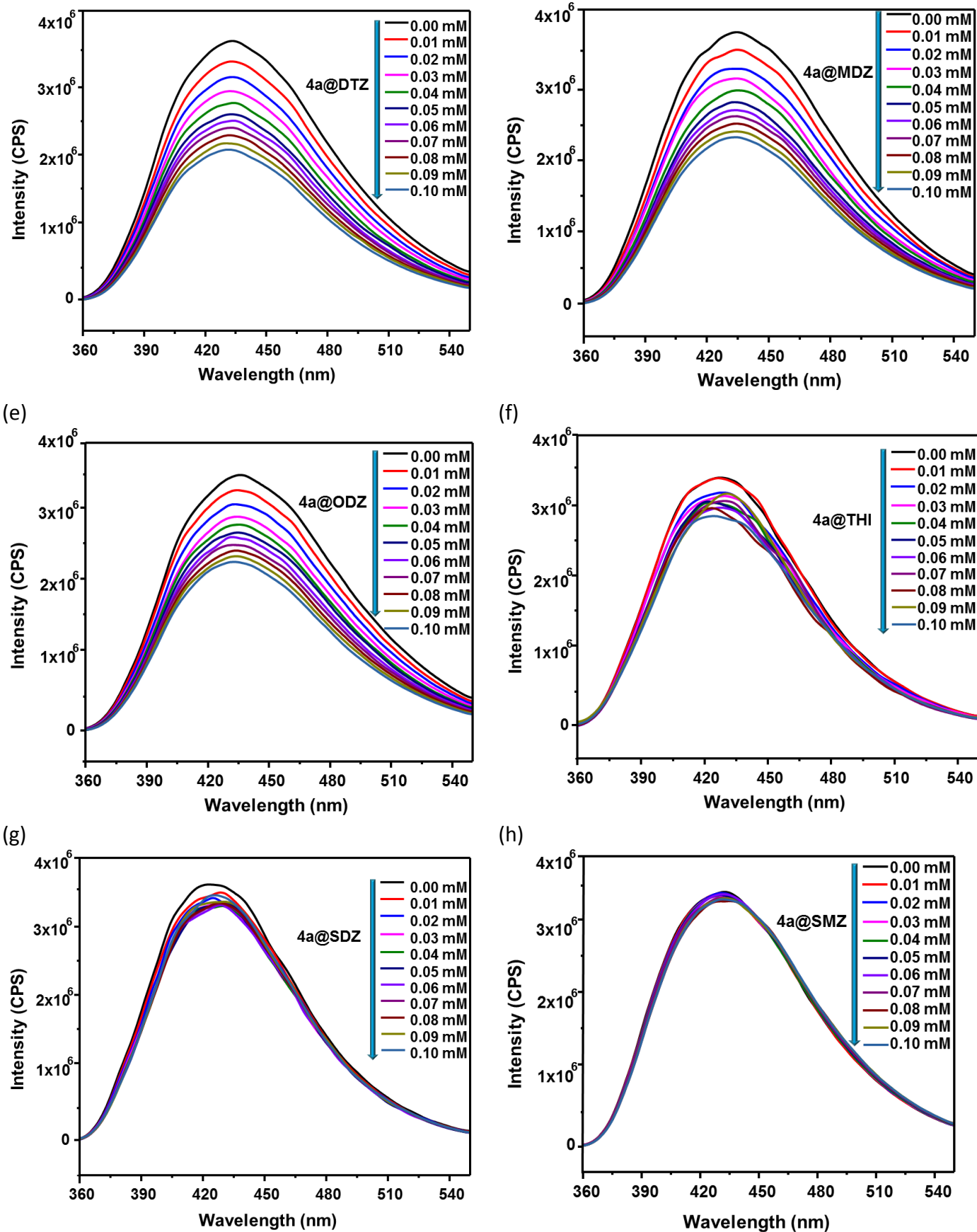


**Fig. S18.** Emission spectra of **4a** upon incremental addition of (a) nitrofurantoin (NFT) (b) furazolidone (FZD) (c) dimetridazole (DTZ) (d) metronidazole (MDZ) (e) ornidazole (ODZ) (f) thiamphenicol (THI) (g) sulfadiazine (SDZ) (h) sulfamethazene (SMZ) solutions (each of 1 mM, 200  $\mu$ L).

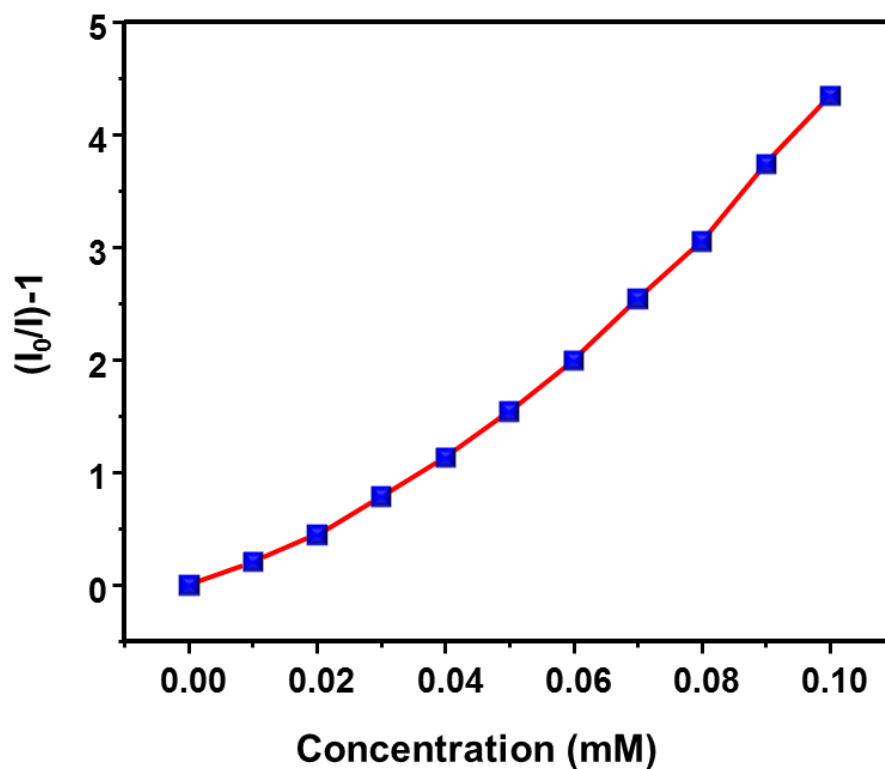


**Fig. S19.** The curvature of the S-V plot for 1 mM NZF solution (0 to 200  $\mu$ L).

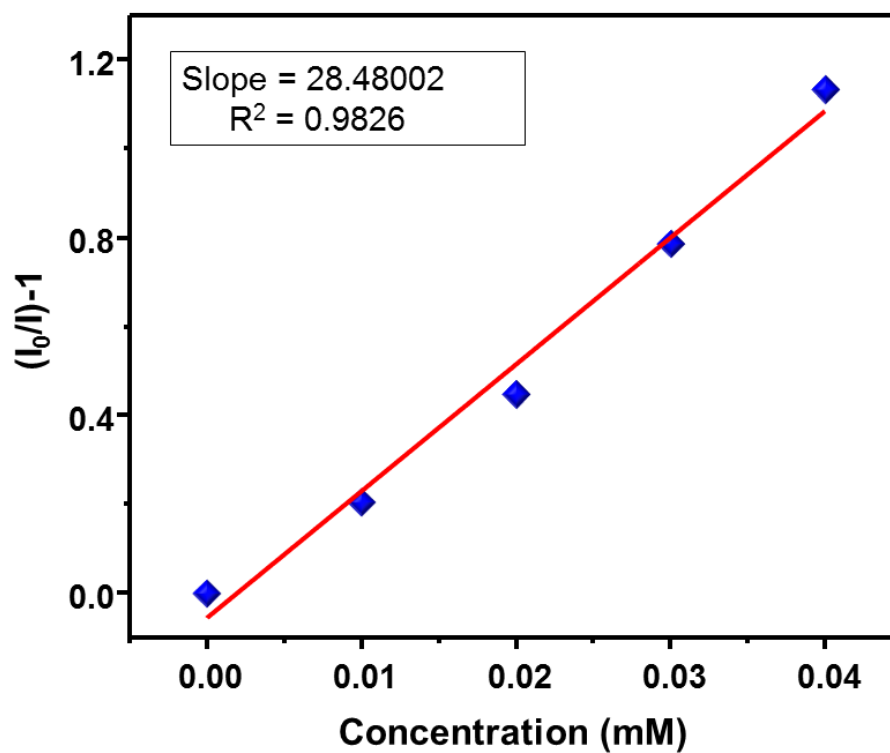


**Fig. S20.** Stern-Volmer (S-V) plot for 1 mM NZF solution (0 to 200  $\mu$ L). The relative fluorescence intensity  $(I_0/I)^{-1}$  is linear with NZF concentration in the range of 0–0.04 mM.

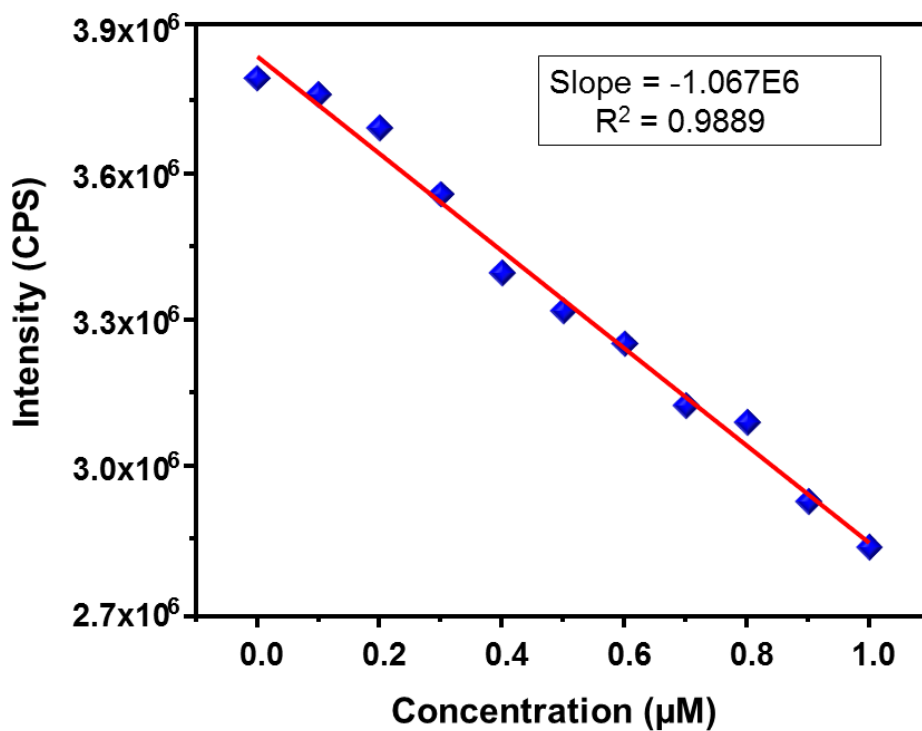


**Fig. S21.** Linear region of fluorescence intensity of **4a** upon addition of NZF (0 – 200  $\mu\text{L}$ , 10  $\mu\text{M}$  stock solution).

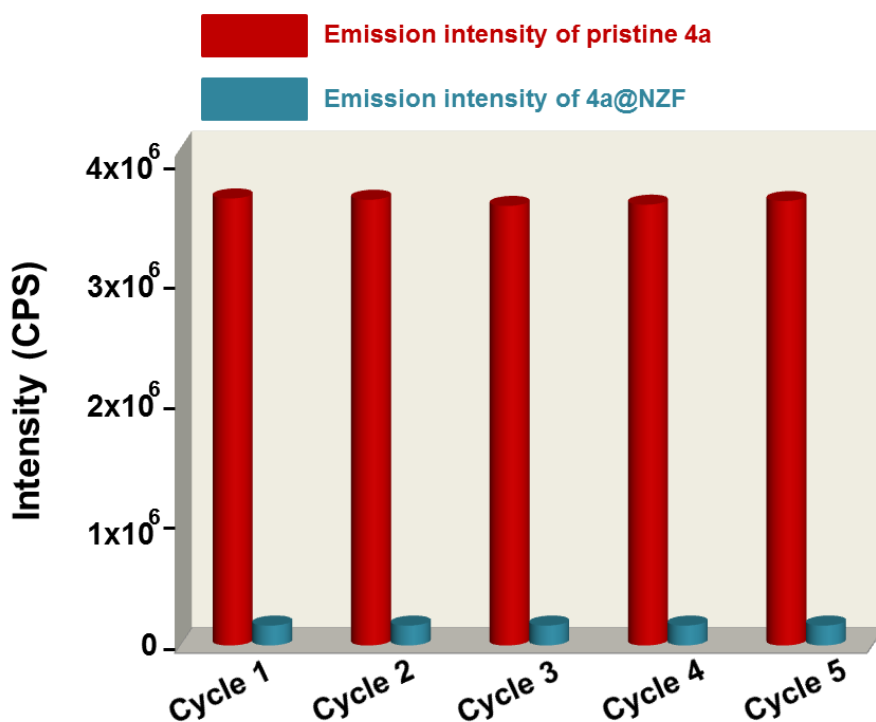


**Fig. S22.** Reproducibility of quenching efficiency of **4a** towards 1 mM NZF solution up to five sensing-recovery cycles.

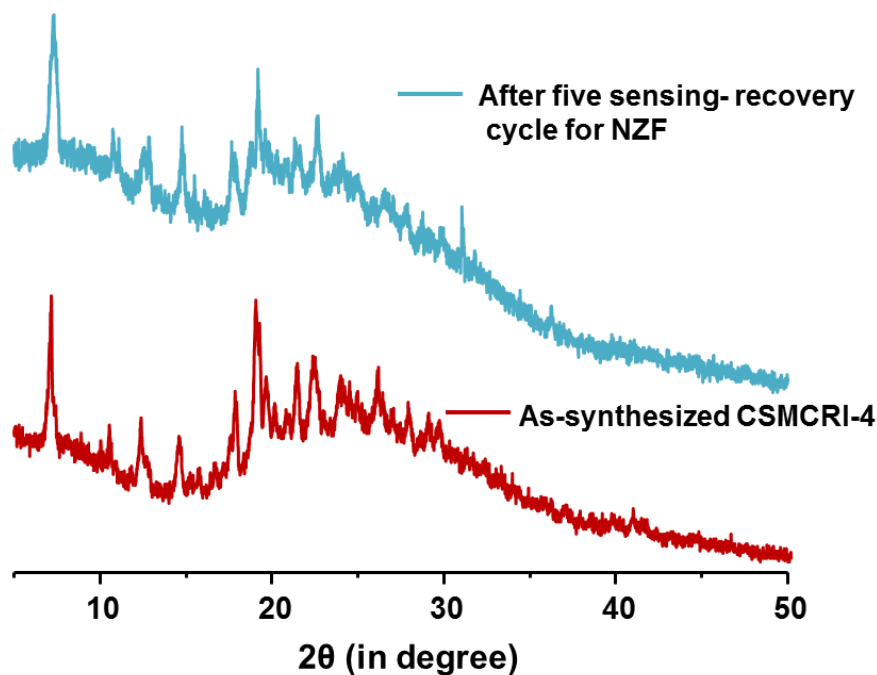


**Fig. S23.** PXRD patterns of **4a** obtained after five sensing-recovery cycles for NZF (1 mM), revealing that structural integrity of the framework is maintained.

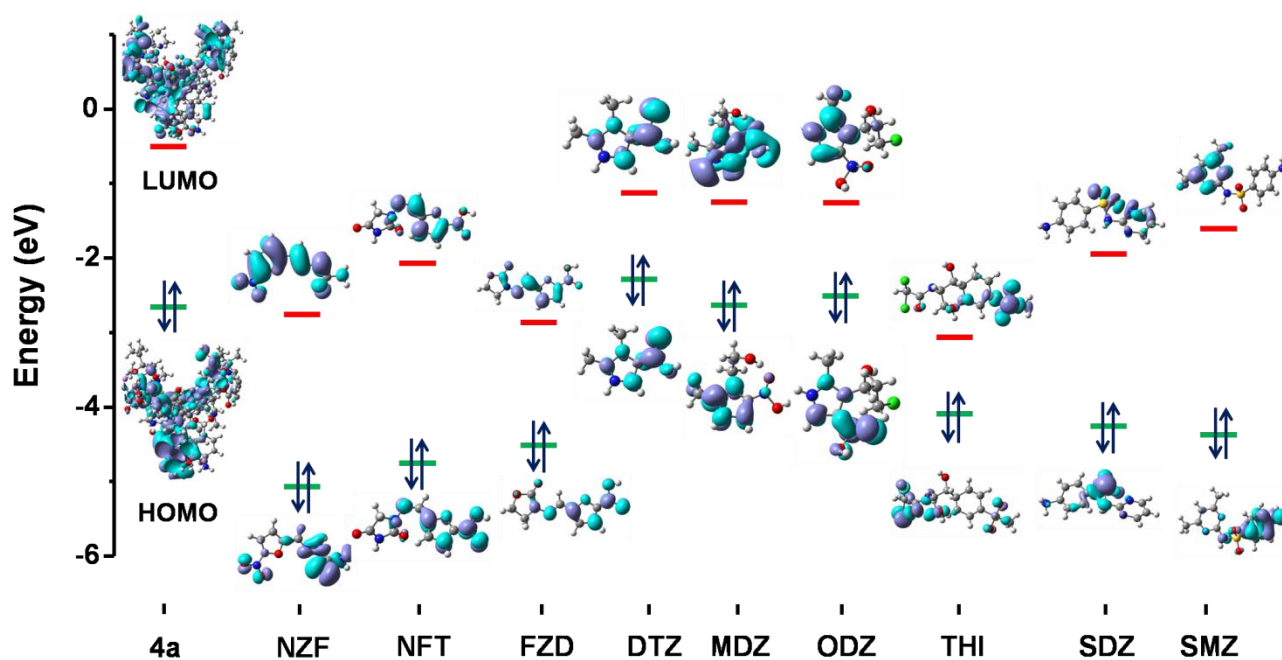


**Fig. S24.** HOMO–LUMO energies for MOF (**4a**) along with the studied antibiotic molecules.

### Computational Modelling Part

**Microscopic models for the bulk 4a framework.** The experimentally refined structure of **4a** was initially considered with the addition of the H atoms on the carbon atoms of the organic linker and the incorporation of  $[(\text{CH}_3)_2\text{NH}_2]^+$  as counter-cation in order to maintain the global charge neutrality of the system. These resulting models were geometry optimized at the Density Functional Theory (DFT) level using the CP2K package.<sup>9-12</sup> In these simulations, the atomic positions of both MOF framework and the

$[(\text{CH}_3)_2\text{NH}_2]^+$  counter-cation were relaxed while the unit cell parameters were kept fixed at the values determined experimentally. All the geometry optimizations were performed using the Perdew-Burke-Ernzerhof (PBE) functional<sup>13,14</sup> along with a combined Gaussian basis set and pseudopotential.<sup>10,12,15</sup> For Carbon, Nitrogen, Oxygen, and Hydrogen, a triple zeta (TZVP-MOLOPT) basis set was considered, while a double zeta (DZVP-MOLOPT) was applied for Lithium.<sup>15</sup> The pseudo potentials used for all atoms were those derived by Goedecker, Teter and Hutter.<sup>16,17</sup> The van der Waals interactions were considered via the use of semi-empirical dispersion corrections as implemented in the DFT-D3 method.<sup>18,19</sup> All the calculations were performed at the  $\Gamma$ -point and Fig. S25 shows the DFT optimized **4a** single crystal structure and Table S9 reports the cell parameters.

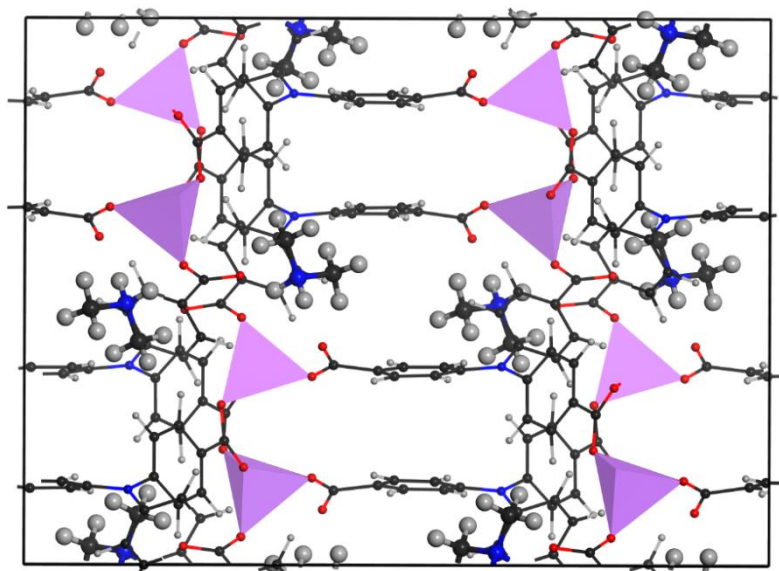
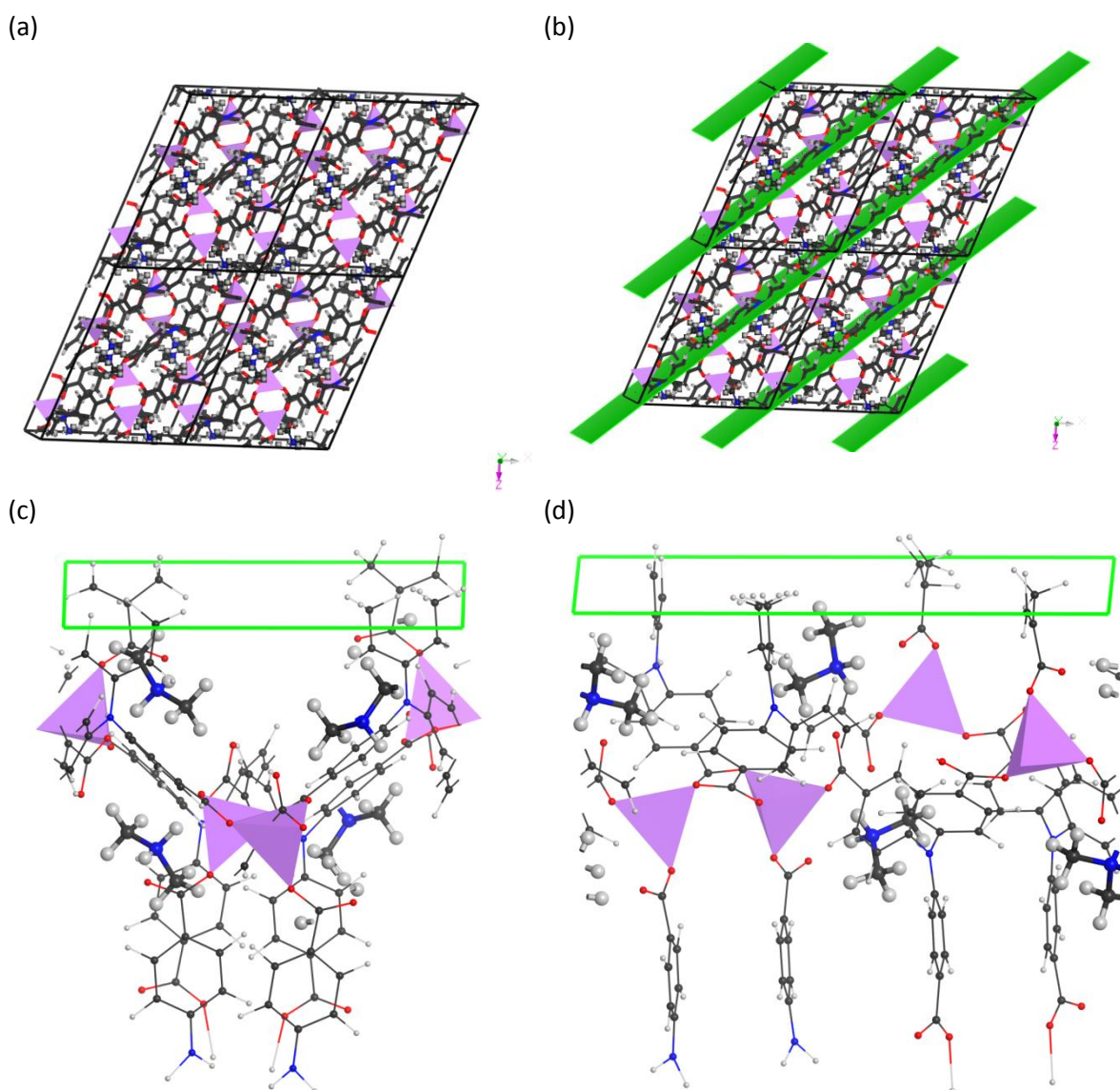


**Fig. S25.** The single unit cell ( $1 \times 1 \times 1$  simulation box) considered for the DFT calculations viewed along  $c$  for **4a**. (Gray, carbon; blue, nitrogen; white, hydrogen; red, oxygen; purple, lithium). For clarity, extra-framework cations are shown in larger ball-stick model.

#### Microscopic models for the MOF surface: (**4a** [101] surface)

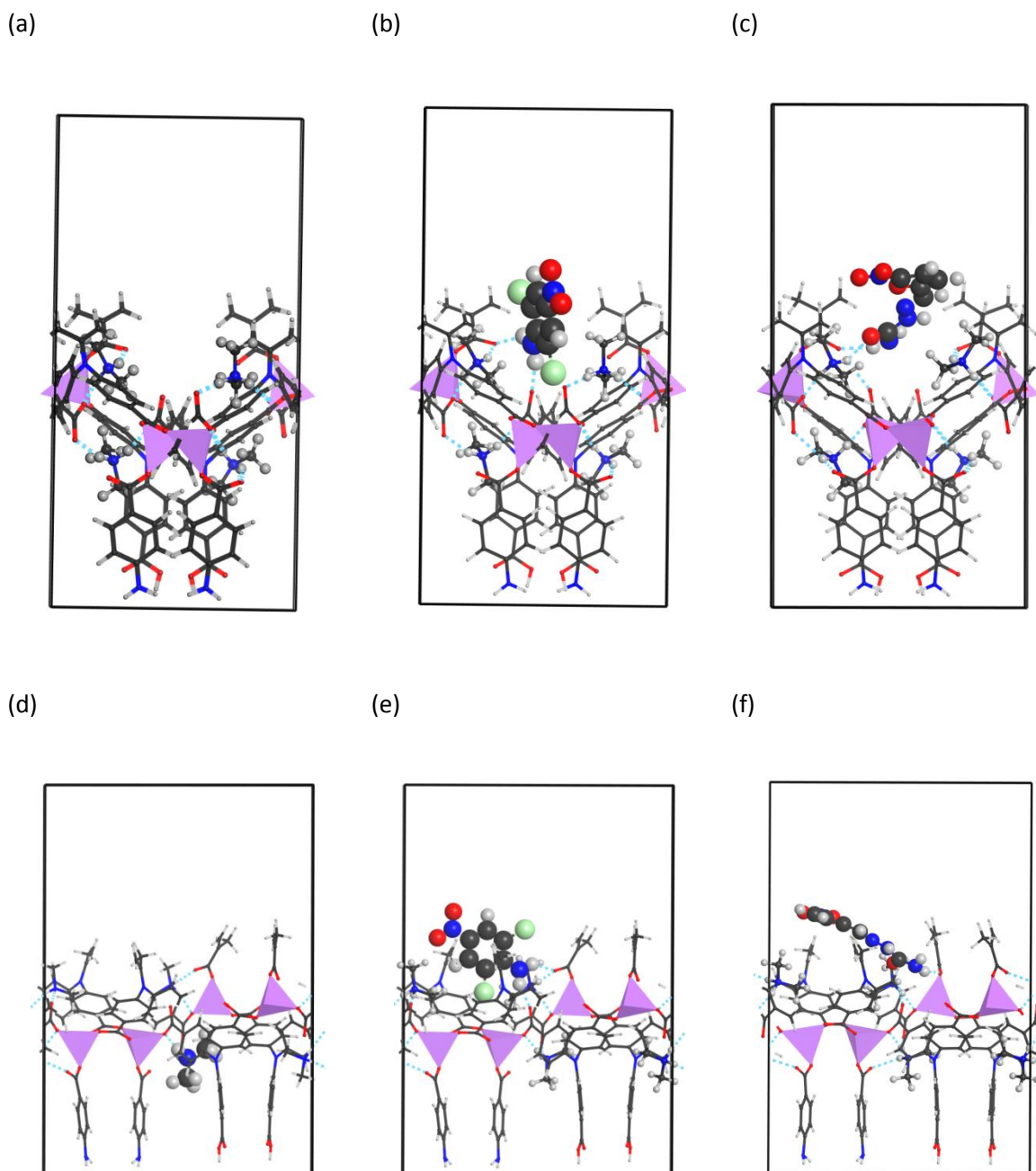
The optimized bulk structure of **4a** was used to identify the sets of Miller indices that would result in a favourable surface, via the Bravais–Friedel–Donnay–Harker method.<sup>20,21</sup> Out of the so-selected Miller indices, the [101] surface was selected for **4a**, since this surface expose the pores to interact guest analytes directly with Li metal ion, effective interactions with the organic linker and  $[(\text{CH}_3)_2\text{NH}_2]^+$  counter-cation, are thus relevant for adsorption and separation applications. A visual inspection and comparison of the faces identified revealed that [101] hkl values gave suitable adsorption of guest to **4a**. Therefore, the calculations were performed using the [101] face, as this was the one most likely to dominate the crystal habit. The planes considered for these cuts are shown in Fig. S25. This **4a** [101] surface was modeled by a  $(1 \times 1)$  slab with 10.0 Å depth from the optimized **4a** single crystal with  $[(\text{CH}_3)_2\text{NH}_2]^+$  as counter-cation, where the surface was initially cleaved by considering half-cell length in the  $b$  direction to reduce the computational const. Models of these surfaces were built considering slab depths of 10 Å of the bulk crystal and the  $(1 \times 1)$  slab model of around 19.88 and 15.24 Å. Further, the [101] surfaces were constructed considering 3D periodic boundary conditions, and their dimensions were of 19.88 and 15.24 Å for  $a$  and  $c$ , respectively and depth of 28.31 Å along the  $b$  direction (the direction perpendicular to the surface slabs, (Fig. S26) for

**4a**. A vacuum layer was inserted along the *b* direction, with a thickness greater than 15 Å, in order to decouple the interactions between periodic images. The net dipole driven by the surface cleavage was eliminated by translating some of the organic linkers from the top to the bottom of the facets. In order to cure the dangling bonds, the organic carbons and carboxylate oxygen were capped with hydrogen atoms. The **4a** [101] surface containing altogether 4 Li, 106 C, 106 H, 10 N and 28 O atoms, and a 15 Å thick vacuum layer above the slab. The final surface model was then geometry-optimized using the Quickstep module of the CP2K package<sup>9-12</sup> and considering the same level of theory and parameters as for the optimization of the bulk model. All the atomic coordinates of the surface models were relaxed and all the calculations were performed at the  $\Gamma$ -point. The final DFT-geometry-optimized **4a** slab model was used to provide a suitable contact surface with the analytes (e.g. DCNA and NZF). Subsequently, the pesticide (e.g DCNA) and antibiotic (e.g NZF) analytes loaded **4a** surface [101] was also geometry optimized with the same level of theory. Finally, the geometry optimized **4a** surface [101] without (Fig. S27a) and with analytes, DCNA (Fig. S27b) and NZF (Fig. S27c), were used to explore the single point energy and further extraction of HOMO and LUMO energy (Table S8) for understanding the optical properties of the pesticide and antibiotics loaded MOF with the same level of theory and parameters as for the optimization of the **4a** surface [101] model.



**Fig. S26.** (a) The super cells ( $2 \times 1 \times 2$ ) DFT optimized **4a** viewed along *c* direction with slight tilting to view properly and (b) the super cells exposing the [101] miller plane (solid green planes) of DFT

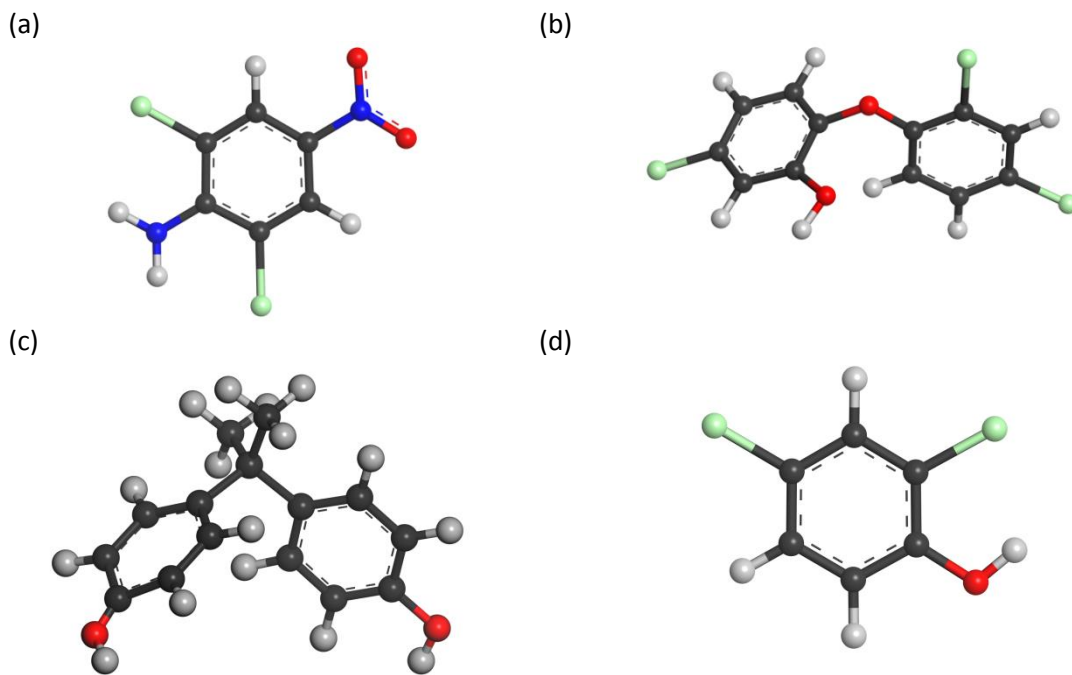
optimized **4a**. The slab cut exposing the [101] miller plane (solid green lines) of **4a**, showing the different orientations (c) along *c* and (d) along *a*. (Gray, carbon; blue, nitrogen; white, hydrogen; red, oxygen; purple, lithium). For clarity, extra-framework cations are shown in larger ball-stick model.



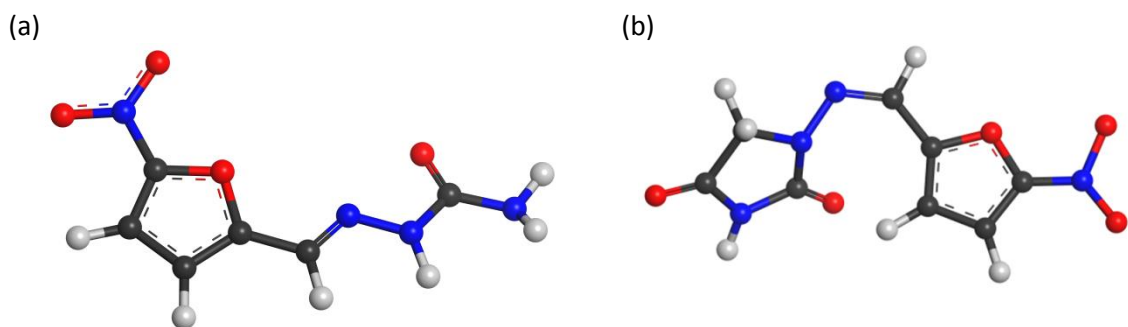
**Fig. S27.** (a), (b) and (c) DFT-optimized **4a** [101] surface, DCNA@**4a** [101] surface and NZF@**4a** [101] surface viewed along *c* direction. (d), (e) and (f) DFT-optimized **4a** [101] surface, DCNA@**4a** [101] surface and NZF@**4a** [101] surface viewed along *a* direction. (Gray, carbon; blue, nitrogen; white, hydrogen; red, oxygen; purple, lithium, Chlorine; green, and hydrogen bonding network represent in dotted cyan line). For clarity, existing cations and respective nitro-organic molecules are shown in larger ball-stick model.

#### Microscopic models for the pesticides and antibiotics

All experimentally investigated pesticides, i.e. DCNA, TCHDE, BHP and DCP, and antibiotics, i.e., NZF, NFT, FZD, MDZ, ODZ, DTZ, THI, SMZ and SDZ were then geometry-optimized using the Quickstep module of the CP2K package.<sup>9-12</sup> and considering the same level of theory and parameters as for the case of **4a** [101] surface. In order to keep the identical plane wave cut off for all calculations, the same periodic boundary conditions of **4a** surface [101] were also used for the geometry optimizations of all pesticides and antibiotics, each molecule was placed at the centre of the simulation box with dimensions as similar to the slab models, i.e. 19.88, 15.24 and 28.31 Å. Figures S28 and S29 shows the DFT-optimized pesticides and antibiotics, respectively. Then, the geometry optimized pesticides and antibiotics were used to explore the single point energy and further extraction of HOMO and LUMO energy, which is reported in Table S6 and Table S7 for all experimentally investigated pesticides and antibiotics, respectively.



**Fig. S28.** DFT optimized pesticides molecules: (a) DCNA, (b) TCHDE, (c) BHP and (d) DCP.



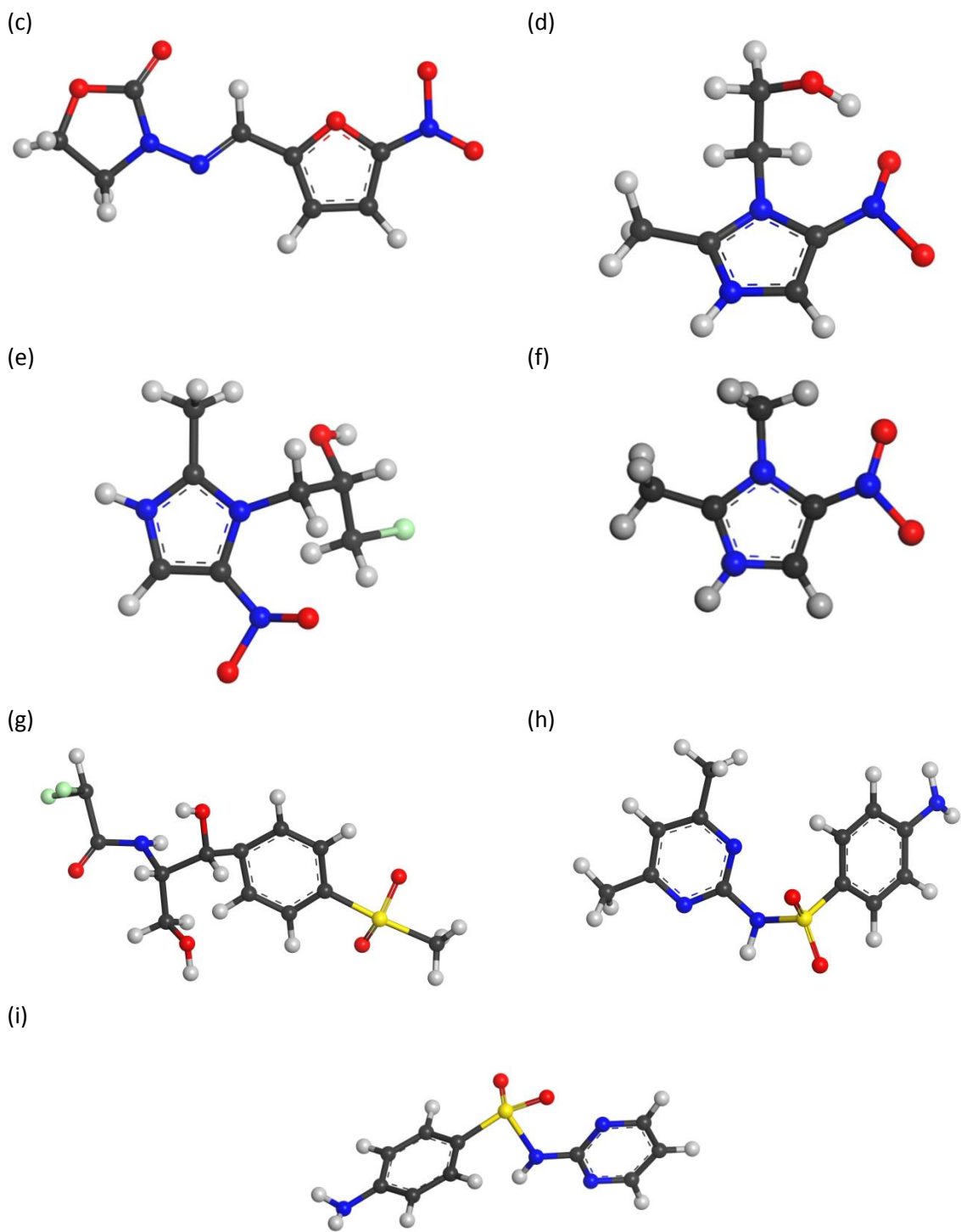


**Fig. S29.** DFT optimized antibiotic molecules: (a) NZF, (b) NFT, (c) FZD, (d) MDZ, (e) ODZ, (f) DTZ, (g) THI, (h) SMZ and (i) SDZ.

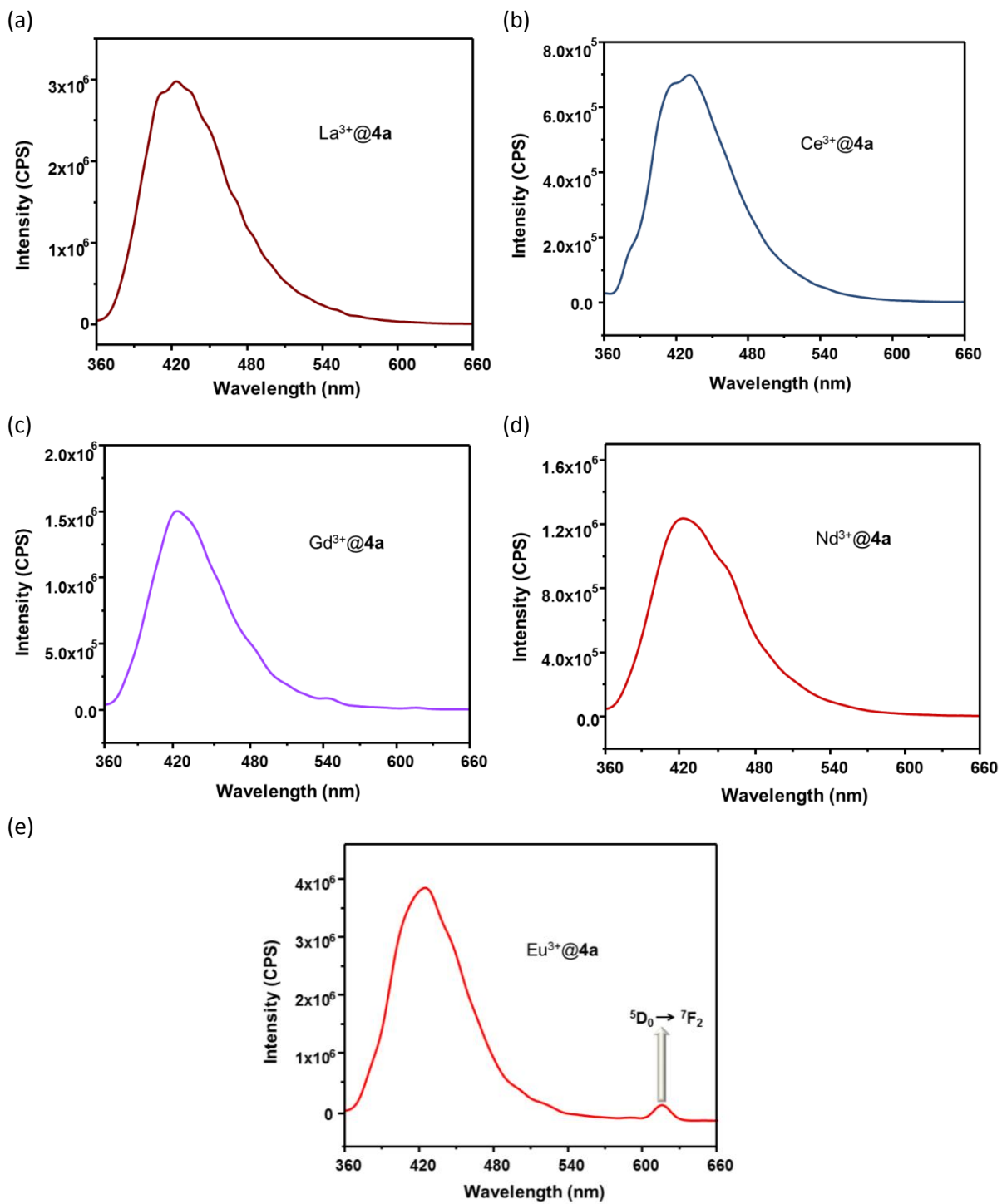


**Fig. S30.** Emission spectra of  $\text{Ln}^{3+}@4\text{a}$ . Ln: (a) La, (b) Ce, (c) Gd, (d) Nd and (e) Eu.

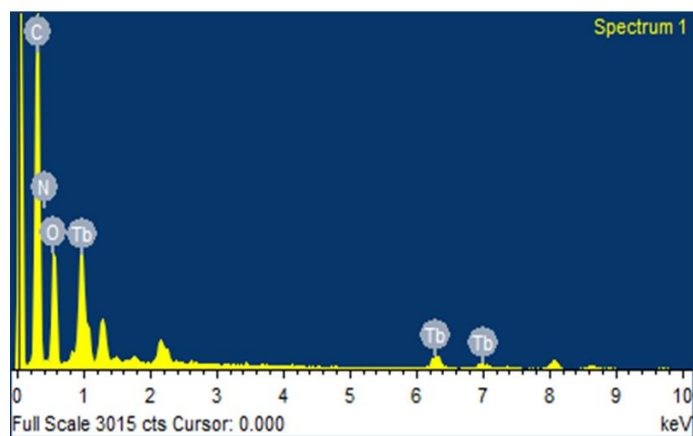


**Fig. S31.** The EDX pattern of Tb<sup>3+</sup>@4a.

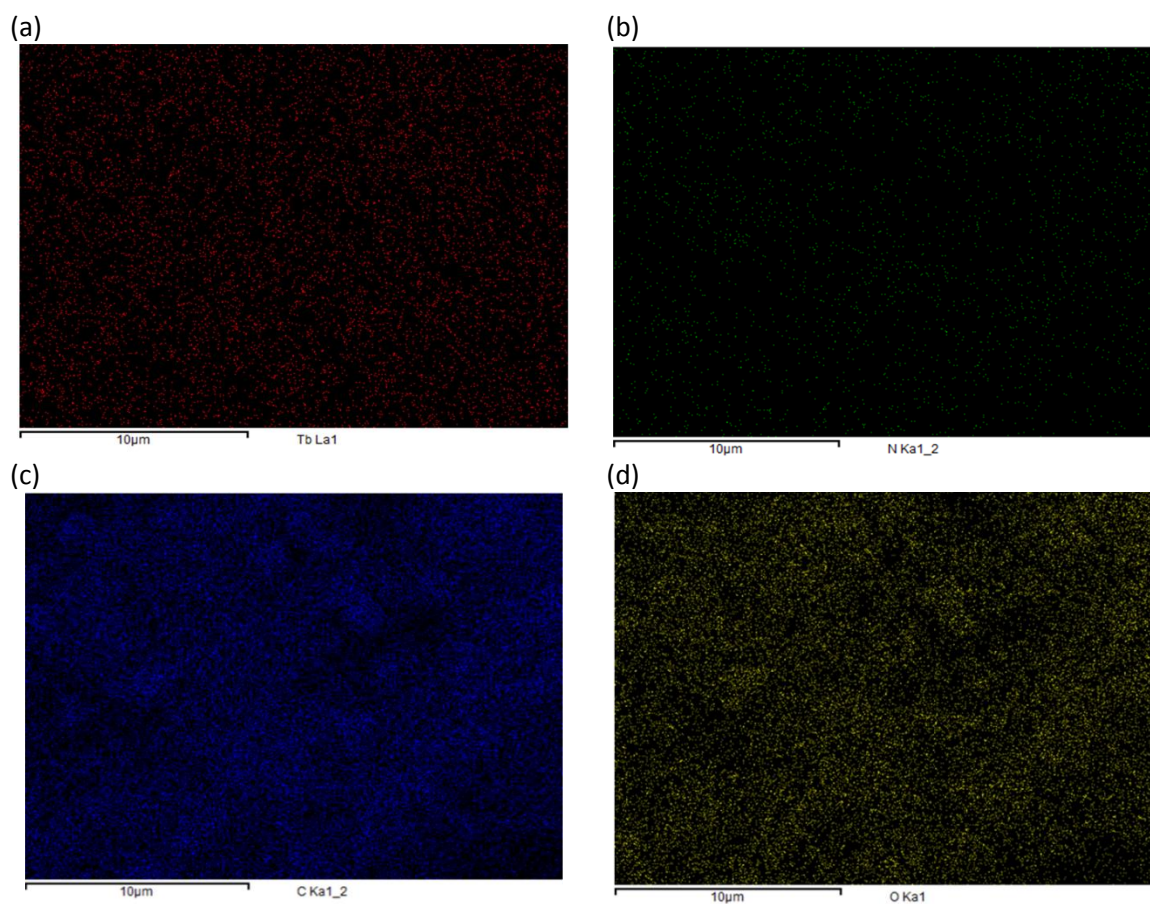


**Fig. S32.** Elemental mapping patterns of Tb<sup>3+</sup>@4a (a) Terbium, (b) Nitrogen, (c) Carbon and (d) oxygen.

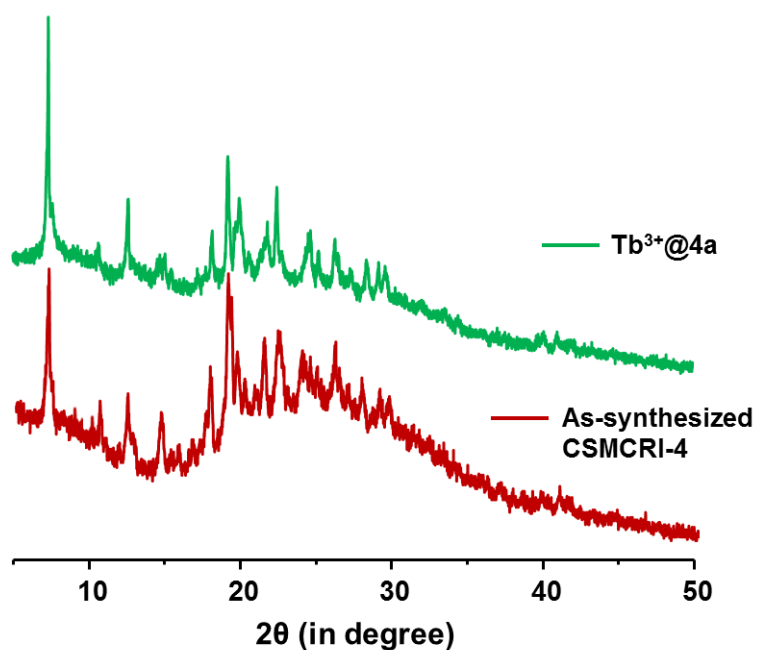


**Fig. S33.** PXRD patterns of 4a obtained after immersing in terbium nitrate solution (10 mM), showing that structural integrity of the framework is maintained.

(a)

(b)

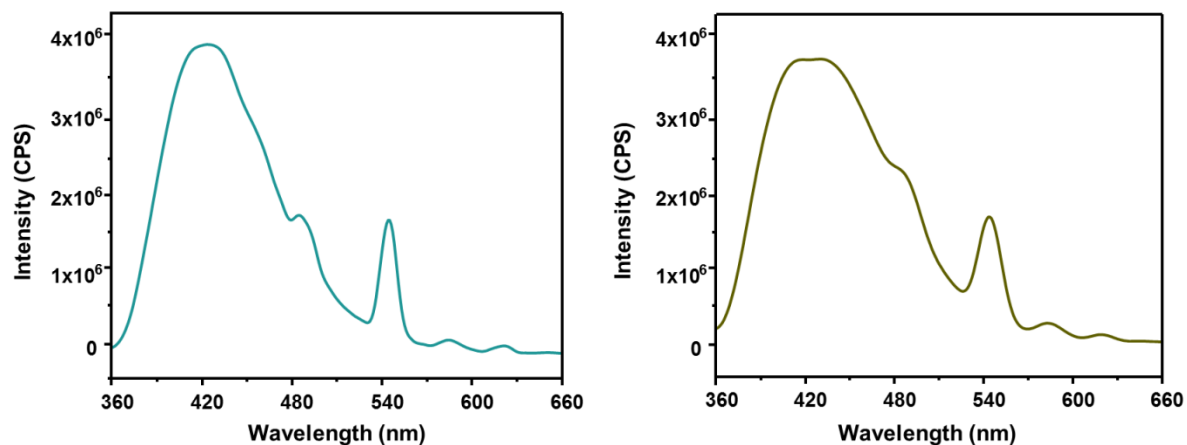


**Fig. S34.** Emission spectra of Tb<sup>3+</sup>@4a after addition of (a) Na<sub>2</sub>EDTA and (b) NH<sub>4</sub>F.

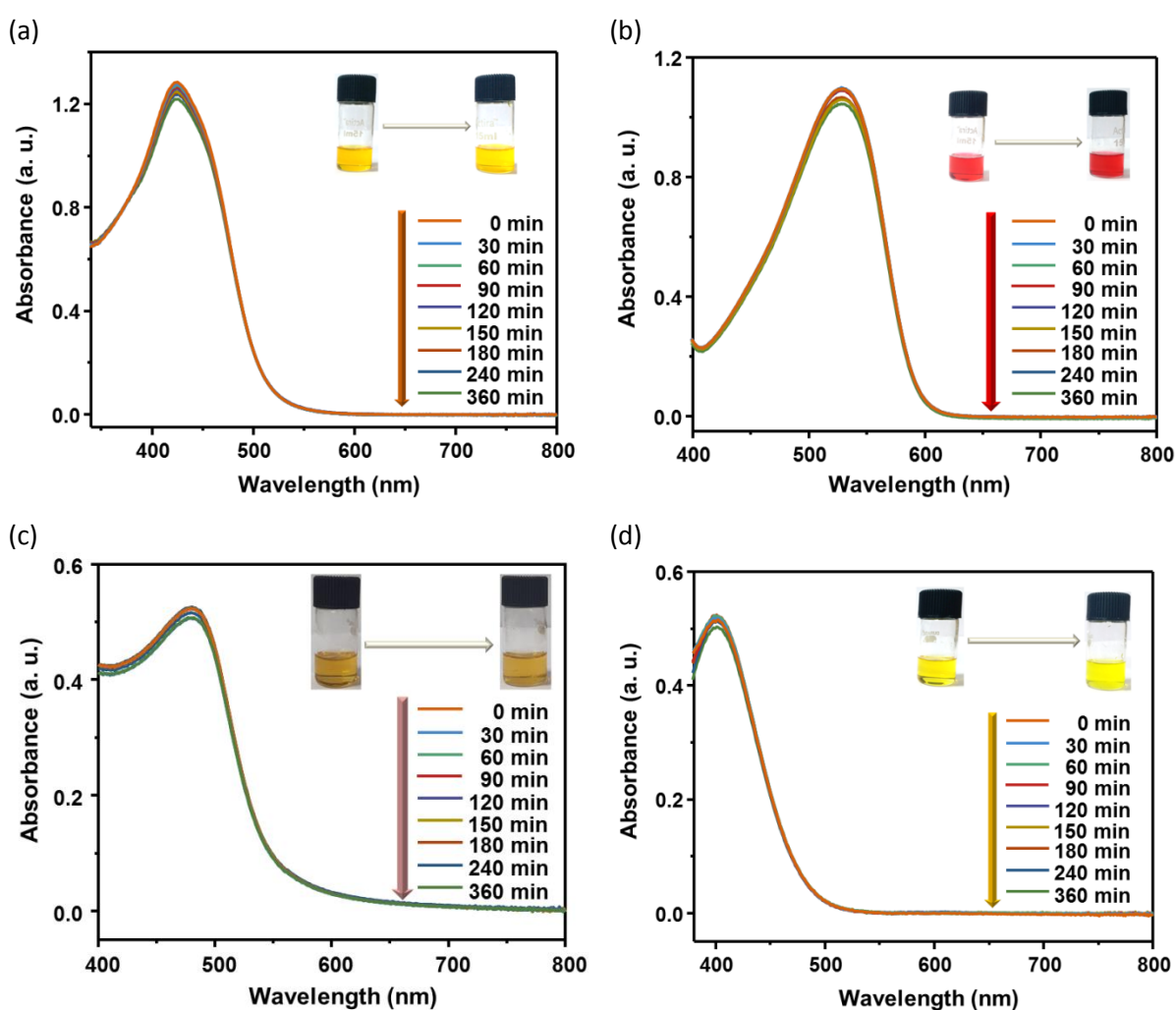


**Fig. S35.** UV-vis spectra of (a) methyl orange (MO<sup>-</sup>) (b) congo red (CR<sup>-</sup>) (c) bismarck brown (BB<sup>0</sup>) (d) thymol blue (TB<sup>0</sup>) solutions in DMF (10 ppm) in presence of 4a monitored at different time intervals. Inset shows the colors of dye solutions before (left) and after (right) the addition of 4a (t = 360 min). The colors persist even upon long term exposure (24 h).

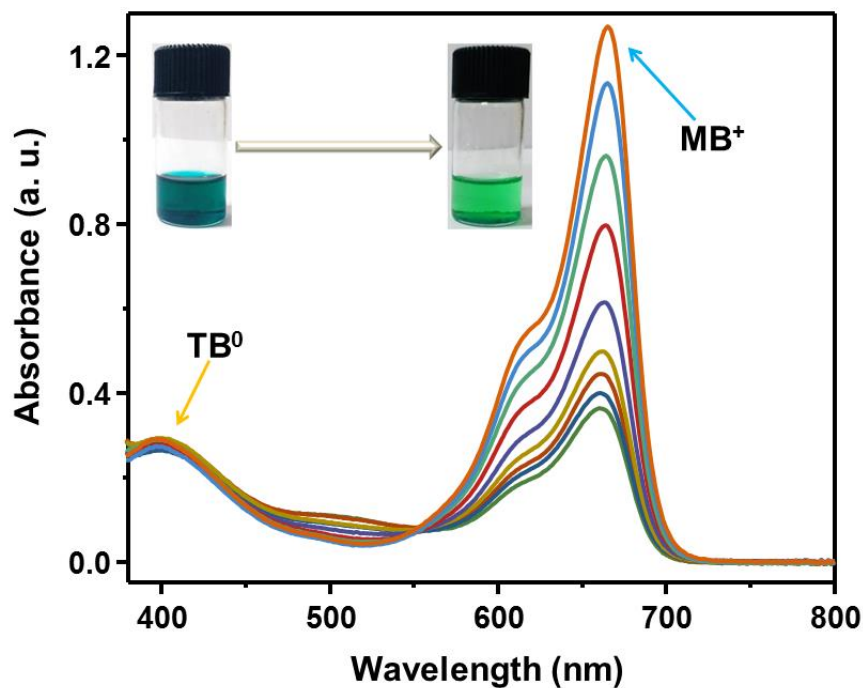


**Fig. S36.** UV-vis spectra of mixed  $\text{MB}^+/\text{TB}^0$  solution in DMF in presence of **4a** monitored at different time intervals.

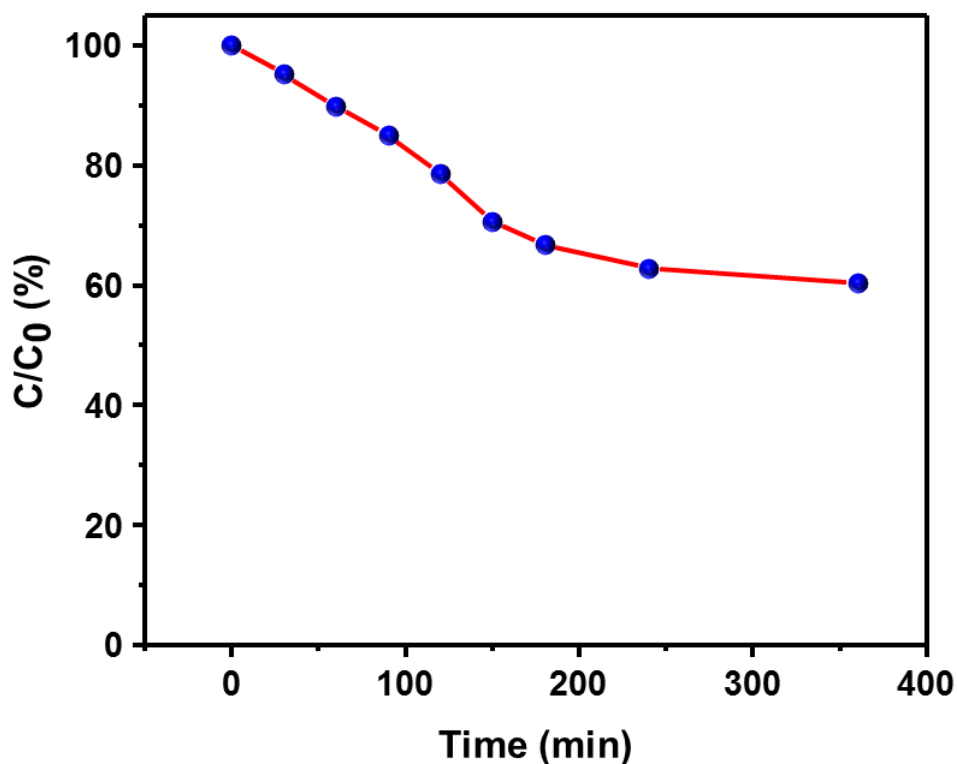
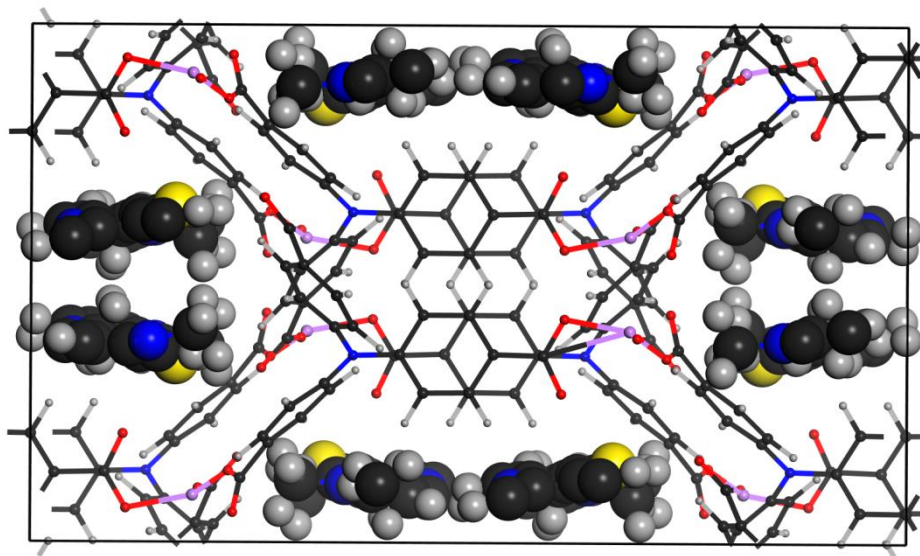


**Fig. S37.** Concentration changes of crystal violet ( $\text{CV}^+$ ) solution with time.

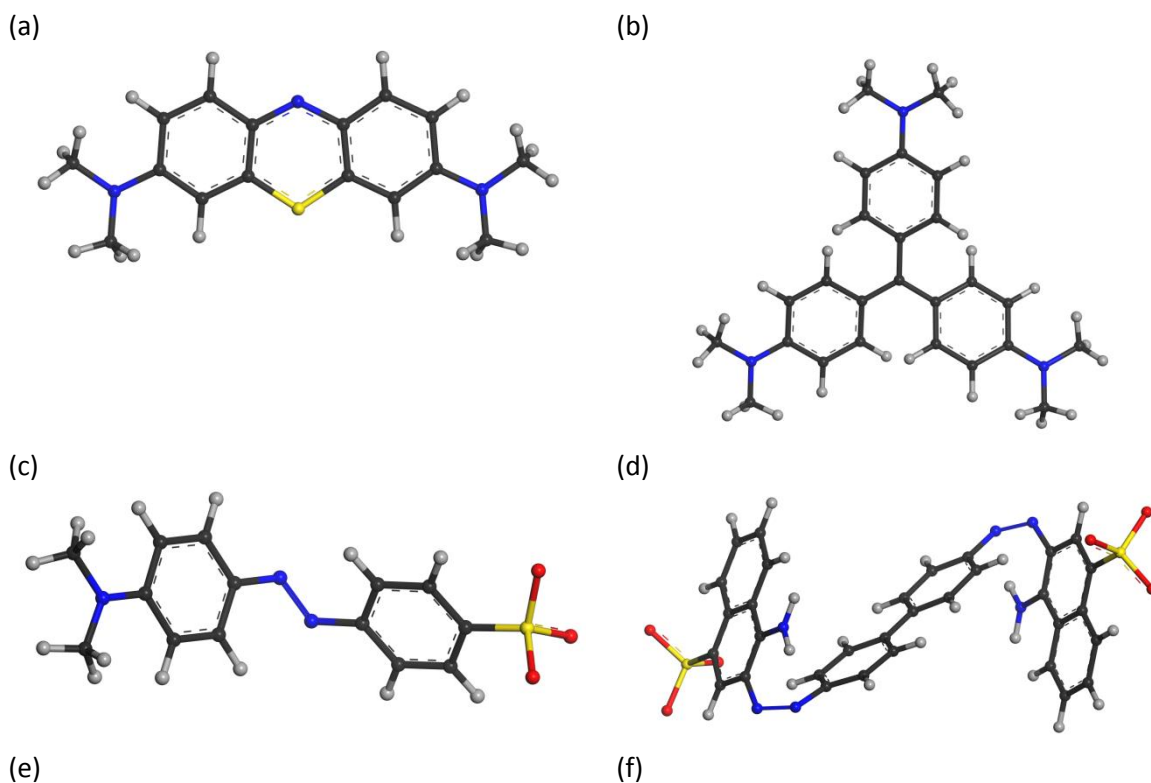
#### Microscopic models for the **4a** framework with organic dyes.

All  $[(\text{CH}_3)_2\text{NH}_2]^+$  extra framework monovalent cation in DFT-optimized structure of **4a** was replaced by  $\text{MB}^+$ , further the structure model was then geometry-optimized using the Quickstep module of the CP2K package<sup>9-12</sup> and considering the same level of theory and parameters as for the optimization of the bulk model. All the atomic coordinates of the surface models were relaxed and all the calculations

were performed at the  $\Gamma$ -point. Also, experimentally investigated common organic dyes, including cationic methylene blue ( $\text{MB}^+$ ) and crystal violet ( $\text{CV}^+$ ); anionic methyl orange ( $\text{MO}^-$ ) and congo red ( $\text{CR}^-$ ); neutral thymol blue ( $\text{TB}^0$ ) and bismarck brown ( $\text{BB}^0$ ) were geometry-optimized using the Quickstep module of the CP2K package<sup>9-12</sup> and considering the same level of theory and parameters as for the case of bulk **4a**. In order to keep the identical plane wave cut off, i. e 500 eV, for all calculations, the same periodic boundary conditions of bulk **4a** were also used for the geometry optimizations, each molecule was placed at the centre of the simulation box with dimensions as similar to the bulk **4a**, i.e. 15.25, 25.19 and 19.88 Å.



**Fig. S38.** DFT-optimized **4a** with  $\text{MB}^+$  viewed along  $c$ . (Gray, carbon; blue, nitrogen; white, hydrogen; red, oxygen; purple, lithium, sulphur; yellow). For clarity, dye molecules are shown in space-fill model.



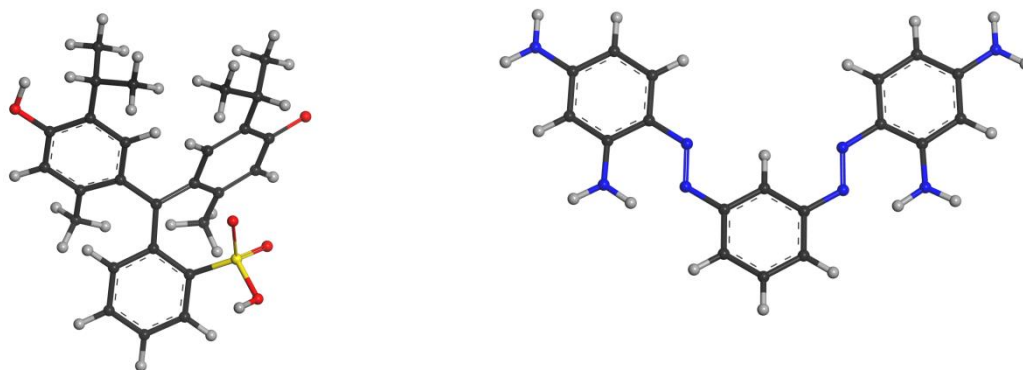


**Fig. S39.** DFT optimized structures of organic dye molecules: (a) MB<sup>+</sup>, (b) CV<sup>+</sup>, (c) MO<sup>-</sup>, (d) CR<sup>-</sup>, (e) TB<sup>0</sup>, and (f) BB<sup>0</sup>.

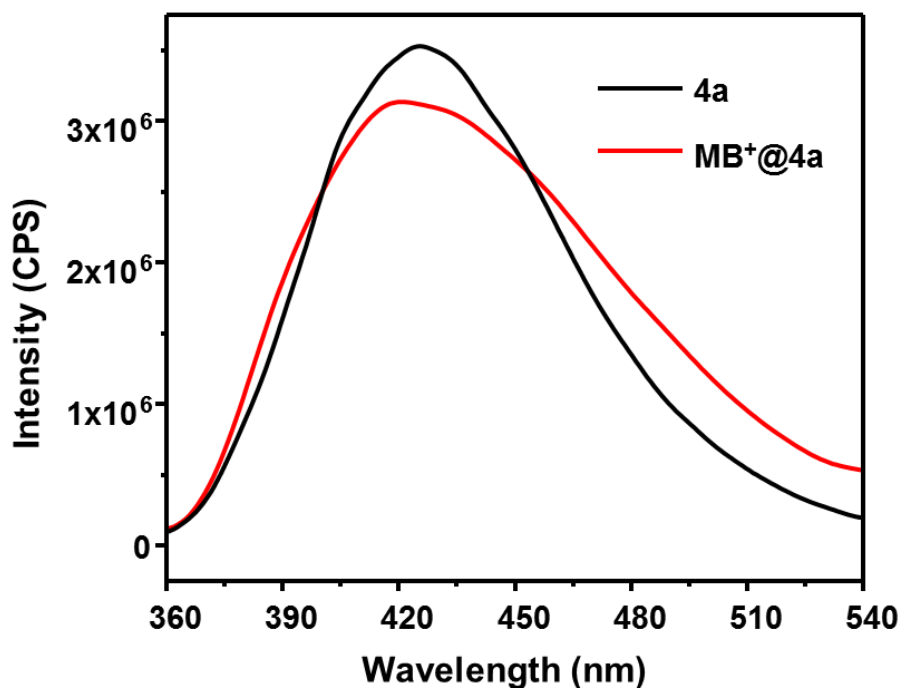


**Fig. S40.** Emission spectra of **4a** (black) and MB<sup>+</sup>@**4a** (red).

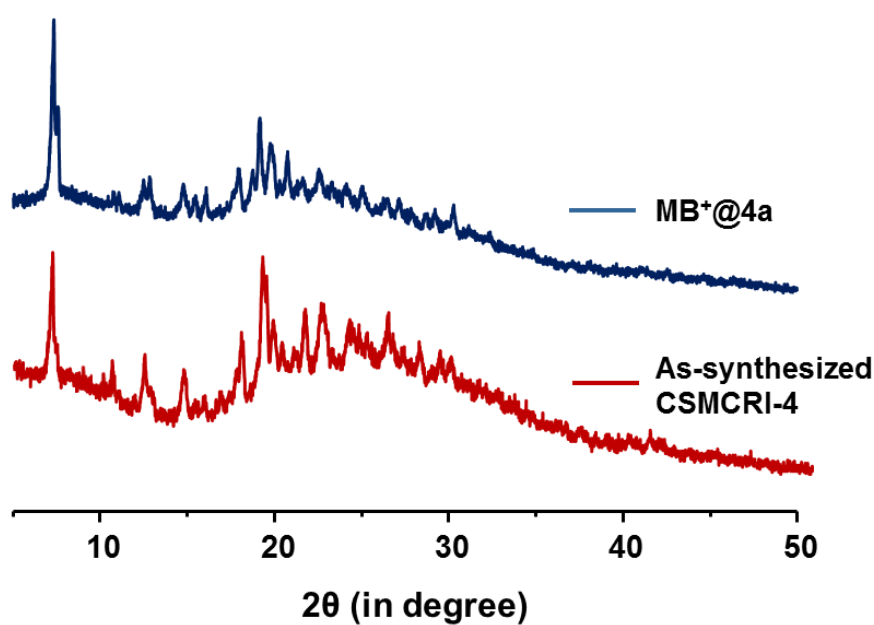


**Fig. S41.** PXRD patterns of **4a** obtained after methylene blue adsorption, showing that structural integrity of the framework is maintained.

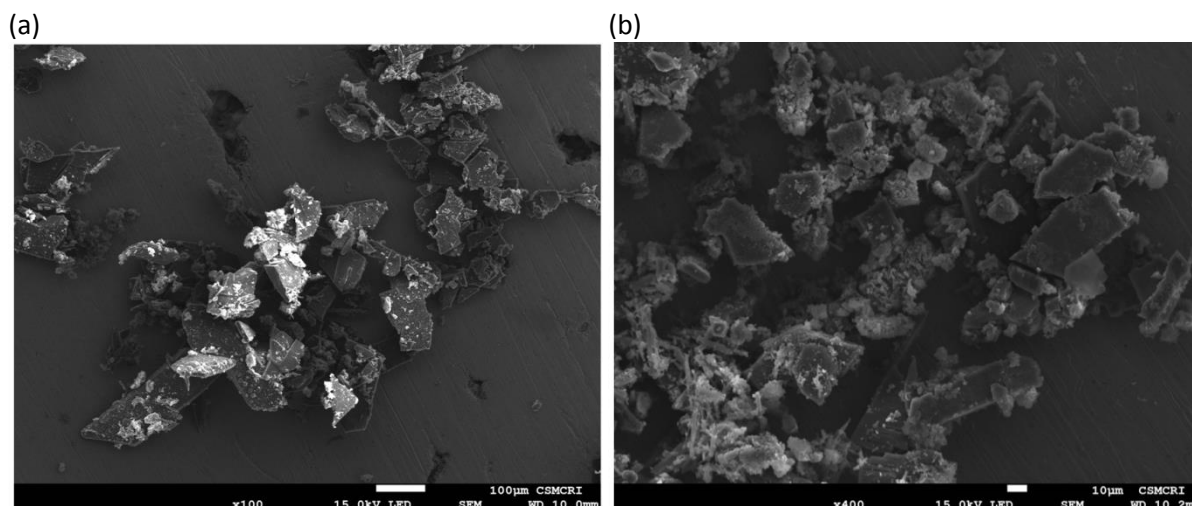


**Fig. S42.** FE-SEM images of (a) pristine **4a** and (b) **4a** after exchange with methylene blue; corroborating unaltered plate-like morphology upon MB<sup>+</sup> dye encapsulation.

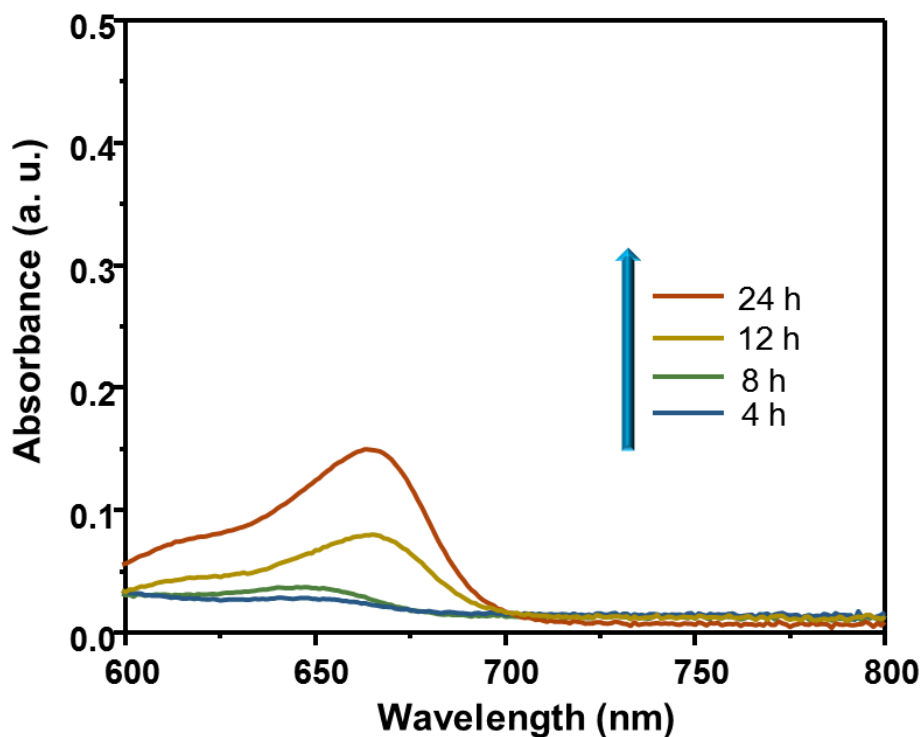


**Fig. S43.** UV-vis spectra of MB<sup>+</sup> release from MB<sup>+</sup>@**4a** in pure DMF.

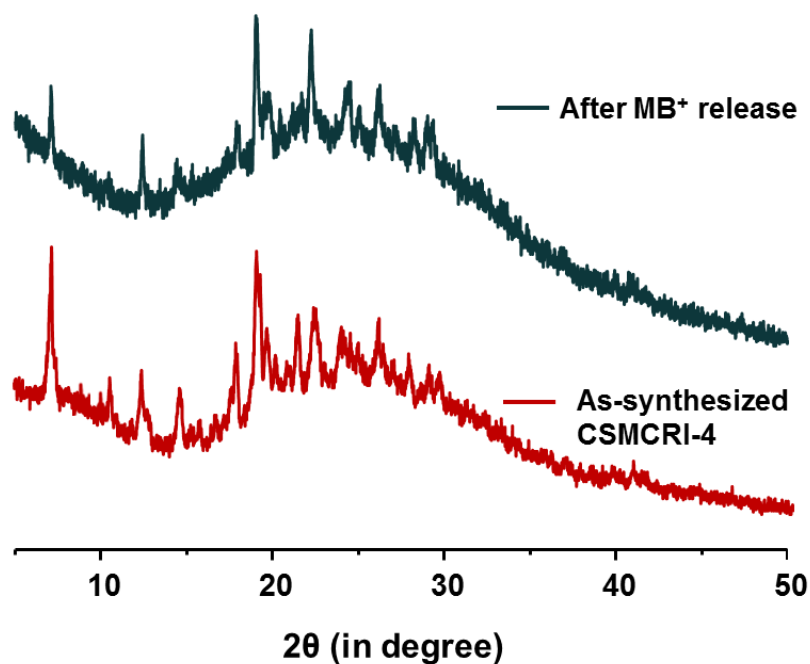


Fig. S44. PXRD patterns of **4a** obtained after methylene blue release.

Table S1. Crystallographic data and refinement parameters for **CSMCRI-4**

Identification code	<b>CSMCRI-4</b>
Empirical formula	$C_{21}H_{12}LiNO_6$
Formula weight	381.26
Temperature/K	118(2)
Crystal system	Monoclinic
Space group	$C2/c$
a/Å	15.8425(19)
b/Å	24.624(3)
c/Å	17.549(2)
$\alpha/^\circ$	90.00
$\beta/^\circ$	111.466(3)
$\gamma/^\circ$	90.00
Volume/Å <sup>3</sup>	6371.0(13)
Z	8
$\rho_{calc}/cm^3$	0.795
$\mu/mm^{-1}$	0.058
F(000)	1568.0
Crystal size/mm <sup>3</sup>	0.24 × 0.20 × 0.18
Radiation	MoK $\alpha$ ( $\lambda = 0.71073$ )
2 $\theta$ range for data collection/ $^\circ$	4.66 to 58.58
Index ranges	$-21 \leq h \leq 21, -32 \leq k \leq 32, -23 \leq l \leq 23$
Reflections collected	67783
Independent reflections	8158 [ $R_{int} = 0.1011, R_{sigma} = 0.2252$ ]
Data/restraints/parameters	8158/0/263
Goodness-of-fit on $F^2$	0.7132
Final R indexes [ $I \geq 2\sigma(I)$ ]	$R_1 = 0.0960, wR_2 = 0.2521$
Final R indexes [all data]	$R_1 = 0.1112, wR_2 = 0.3067$
Largest diff. peak/hole / e Å <sup>-3</sup>	1.0081/-0.7030

Alert level A: PLAT026\_ALERT\_3\_ARatio Observed / Unique Reflections (too) Low .. 26 % check

**Explanation:** Diffraction data was not so good due to poor quality of single crystals, and this alert was generated.

Alert level B:

PLAT097\_ALERT\_2\_B Large Reported Max. (Positive) Residual Density 1.01 eA-3  
 PLAT230\_ALERT\_2\_B Hirshfeld Test Diff for O001 --C00C .9.0 s.u.  
 PLAT230\_ALERT\_2\_B Hirshfeld Test Diff for C009 --C00B .8.3 s.u.  
 PLAT230\_ALERT\_2\_B Hirshfeld Test Diff for C00D --C00H .7.5 s.u.  
 PLAT230\_ALERT\_2\_B Hirshfeld Test Diff for C00D --C00K .11.0 s.u.  
 PLAT230\_ALERT\_2\_B Hirshfeld Test Diff for C00D --C00M .14.2 s.u.  
 PLAT230\_ALERT\_2\_B Hirshfeld Test Diff for C00H --C00I .14.2 s.u.  
 PLAT230\_ALERT\_2\_B Hirshfeld Test Diff for C00N --C00S .7.2 s.u.

**Explanation:** These alerts were generated probably due to disorderness in the crystal structure.

**Table S2.** Calculation of standard deviation of fluorescence intensity and limit of detection for **4a** towards dichloran (DCNA)

Blank Readings (4a)	Fluorescence Intensity(CPS)
Reading 1	3800368.55
Reading 2	3520270.27
Reading 3	3505528.26
Reading 4	3446560.2
Reading 5	3225429.98
<b>Standard Deviation (<math>\sigma</math>)</b>	205491.2044
<b>Slope from Graph (K)</b>	$9.9 \times 10^5 \mu\text{M}^{-1}$
<b>Detection limit (<math>3\sigma/K</math>)</b>	0.62 $\mu\text{M}$
<b>Limit of Detection (LOD)</b>	0.23 ppm

**Table S3.** Calculation of standard deviation of fluorescence intensity and limit of detection for **4a** towards NZF

Blank Readings (4a)	Fluorescence Intensity(CPS)
Reading 1	3800368.55
Reading 2	3520270.27
Reading 3	3505528.26
Reading 4	3446560.2
Reading 5	3225429.98
<b>Standard Deviation (<math>\sigma</math>)</b>	205491.2044
<b>Slope from Graph (K)</b>	$1.06 \times 10^6 \mu\text{M}^{-1}$
<b>Detection limit (<math>3\sigma/K</math>)</b>	0.5 $\mu\text{M}$
<b>Limit of Detection (LOD)</b>	0.19 ppm

**Table S4.** A comparison of quenching constant, their LOD values, of various luminescent MOFs used for detection of DCNA

Sl. No.	LMOF/ Coordination Polymer	Quenching constant (M <sup>-1</sup> )	Limit of Detection (LOD)	Medium used	Ref.
1.	{Zn <sub>4</sub> (TPOM)(1,4-NDC) <sub>4</sub> } <sub>n</sub>	2.74 × 10 <sup>4</sup>	0.28 ppm	water	<i>ACS Appl. Mater. Interfaces</i> <b>2018</b> , 10, 42406–42416
2.	[Zn <sub>2</sub> (bpdc) <sub>2</sub> (BPyTPE)]	-	0.13 ppm	DCM	<i>Chem. Commun.</i> <b>2017</b> , 53, 9975–9978
3.	[Zn <sub>2</sub> (L) <sub>2</sub> (TPA)]. 2H <sub>2</sub> O	2.36 × 10 <sup>4</sup>	0.39 ppm	Methanol	<i>New J. Chem.</i> <b>2019</b> , 43, 2353–2361
4.	[Zn <sub>3</sub> (DDB)(DPE)]·H <sub>2</sub> O	3.3×10 <sup>4</sup>	166 ppb	water	<i>Dalton Trans.</i> , <b>2019</b> , 48, 16776–16785
5.	[Cd <sub>3</sub> (CBCD) <sub>2</sub> (DMA) <sub>4</sub> (H <sub>2</sub> O) <sub>2</sub> ].10DMA	4.47 × 10 <sup>4</sup>	145 ppb	DMA	<i>Dalton Trans.</i> <b>2019</b> , 48, 2683–2691
6.	[Mg <sub>2</sub> (APDA) <sub>2</sub> (H <sub>2</sub> O) <sub>3</sub> ].5DMA.5H <sub>2</sub> O	7.50 × 10 <sup>4</sup>	150 ppb	DMF	<i>Inorg. Chem.</i> <b>2018</b> , 57, 13330–13340
7.	[Ag(CIP <sup>-</sup> )]	5.2 × 10 <sup>4</sup>	105 ppb	DMF	<i>Dalton Trans.</i> <b>2019</b> , 48, 10892–10900
8.	<b>CSMCRI-4</b>	2.634 × 10 <sup>4</sup>	0.23 ppm	DMF	<b>This work</b>

**Table S5.** A comparison of quenching constant, their LOD values, of various luminescent MOFs used for detection of NZF

Sl. No.	LMOF/ Coordination Polymer	Quenching constant (M <sup>-1</sup> )	Limit of Detection (LOD)	Medium used	Ref.
1.	[Mg <sub>2</sub> (APDA) <sub>2</sub> (H <sub>2</sub> O) <sub>3</sub> ].5DMA.5H <sub>2</sub> O	9.00 × 10 <sup>4</sup>	108 ppb	DMF	<i>Inorg. Chem.</i> <b>2018</b> , 57, 13330–13340
2.	[Cd <sub>3</sub> (CBCD) <sub>2</sub> (DMA) <sub>4</sub> (H <sub>2</sub> O) <sub>2</sub> ].10DMA	9.72 × 10 <sup>4</sup>	85 ppb	DMA	<i>Dalton Trans.</i> <b>2019</b> , 48, 2683–2691
3.	BUT-12 BUT-13	1.1 × 10 <sup>5</sup> 7.5 × 10 <sup>4</sup>	58 ppb 90 ppb	water	<i>J. Am. Chem. Soc.</i> <b>2016</b> , 138, 6204–6216
4.	{[Eu <sub>2</sub> (BCA) <sub>3</sub> (H <sub>2</sub> O)(DMF) <sub>3</sub> ].0.5DMF·H <sub>2</sub> O} <sub>n</sub>	2.2 × 10 <sup>4</sup>	0.16 μM	water	<i>Chem. Eur. J.</i> <b>2017</b> , 23, 10293 – 10300
5.	[(Zn <sub>4</sub> O) <sub>2</sub> (PDDA) <sub>6</sub> (H <sub>2</sub> O) <sub>2</sub> ].10DMF	6.08 × 10 <sup>4</sup>	NA	DMF	<i>Cryst. Growth Des.</i> <b>2019</b> , 19, 5228–5236
6.	TMPyPE@bio-MOF-1	4.48 × 10 <sup>4</sup>	0.11 ppm	water	<i>J. Mater. Chem. C</i> , <b>2019</b> , 7, 8383–8388
7.	{[Tb(TATMA)(H <sub>2</sub> O)·2H <sub>2</sub> O] <sub>n</sub> }	3.0 × 10 <sup>4</sup>	NA	water	<i>Inorg. Chem.</i> <b>2019</b> , 58, 7746–7753
8.	[NaCd <sub>2</sub> (L)(BDC) <sub>2.5</sub> ].9H <sub>2</sub> O	5.06 × 10 <sup>4</sup>	162 ppb	DMF	<i>J. Mater. Chem. A</i> , <b>2017</b> , 5, 15797–15807
9.	{[Zn <sub>2</sub> (Py <sub>2</sub> TTz) <sub>2</sub> (BDC) <sub>2</sub> ].2(DMF)·0.5(H <sub>2</sub> O)} <sub>n</sub>	1.726 × 10 <sup>4</sup>	0.91 μM	water	<i>Cryst. Growth Des.</i> <b>2018</b> , 18, 7173–7182
10.	<b>CSMCRI-4</b>	2.848 × 10 <sup>4</sup>	0.19 ppm	DMF	<b>This work</b>

**Table S6.** HOMO and LUMO energy levels of different pesticides calculated by density functional theory (DFT) using CP2K package

Analytes	HOMO (eV)	LUMO (eV)	Energy gap (eV)
DCNA	-5.15	-2.61	2.54
TCHDE	-2.38	-0.99	1.39
BHP	-2.69	-0.39	2.30
DCP	-4.63	-1.48	3.15

**Table S7.** HOMO and LUMO energy levels of different antibiotics calculated by density functional theory (DFT) using CP2K package

Analytes	HOMO (eV)	LUMO (eV)	Energy gap (eV)
NZF	-5.06	-2.75	2.31
NFT	-4.74	-2.07	2.67
FZD	-4.51	-2.86	1.65
DTZ	-2.28	-1.12	1.16
MDZ	-2.63	-1.24	1.39
ODZ	-2.50	-1.25	1.25
THI	-4.09	-3.06	1.03
SDZ	-4.25	-1.94	2.31
SMZ	-4.37	-1.60	2.77

**Table S8.** HOMO and LUMO energy levels of **4a**, DCNA@**4a** and NZF@**4a** calculated by density functional theory (DFT) using CP2K package

Analytes	HOMO (eV)	LUMO (eV)	Energy gap (eV)
DCNA@MOF	-2.31	-1.11	1.20
NZF @ MOF	-2.40	-1.62	0.78
MOF ( <b>4a</b> )	-2.65	-0.50	2.15

**Table S9.** Cell parameters of **4a** obtained by DFT optimization

MOF	Lattice Sizes (Å)			Angles(°)			Cell Volume (Å) <sup>3</sup>
	a	b	c	α	β	γ	
<b>4a</b>	15.25	25.19	19.88	90.00	111.47	90.00	7107.86

**Determination of formula & solvent composition of CSMCRI-4 from PLATON Squeeze and Thermogravimetric analysis data:**

From the TGA plot of as-synthesized **CSMCRI-4**, the observed mass loss is 26.62 %

From PLATON Squeeze program void electron count comes out to be 662.6

As **CSMCRI-4** is crystallized in monoclinic space group C2/c (Z=8); so, number of void electron count per unit cell will be  $662.6/8 = 82.8$

As the framework is di-negative, so the void space should be occupied by counter-cations and lattice solvent molecules.

Now, formula of the asymmetric unit excluding all guests is  $[\text{Li}(\text{TCA})]^{2-}$ , and mass of this asymmetric unit is 381.27

**Table S10.** Number of electrons and molecular mass of cation as well as guest molecules associated with **CSMCRI-4** for determination of solvent composition and molecular formula

	Dimethyl formamide (DMF)	Dimethylammoniumcation	Water
No. of electrons	40	26	10
mass	73	46	18

Considering the above mentioned number of electrons, the best possible combination of solvent molecules and cations for **CSMCRI-4** could be  $(\text{Me}_2\text{NH}_2)_2[\text{Li}(\text{TCA})] \cdot 0.5\text{DMF} \cdot \text{H}_2\text{O}$

The total number of electrons contributed by lattice solvent molecules and guest cations will be  $[(26 \times 2) + (40/2) + 10] = 82$ , which is in complete agreement with the PLATON result and thus validates the above formula.

The aforementioned combination was further cross-checked from TGA analysis.

Total mass loss due to solvents and cations is  $[(46 \times 2) + (73/2) + 18] = 146.5$

Therefore total mass of **CSMCRI-4** including all the guests is  $(381.26 + 146.5) = 527.76$

So mass loss due to solvents and guest cations is  $[(146.5/527.76) \times 100] \% = 27.7 \%$ , which is in good agreement with that of the TGA result.

**Table S11.** ICP-OES results for  $\text{Tb}^{3+}$ @**4a**

Sample	Amount of Li	Amount of Tb
$\text{Tb}^{3+}$ @ <b>4a</b>	12.36 mg/L	3.59 mg/L

0.09 mL test solution diluted to 10 mL contains 12.36 mg/L of  $\text{Li}^+$

1 mL test solution contains  $(12.36/0.09 \times 10) = 13.73$  mg/L of  $\text{Li}^+$

Again, 1 mL test solution contains 3.59 mg/L of  $\text{Tb}^{3+}$

So, to find out the amount of  $\text{Tb}^{3+}$  present per 100 mg/L  $\text{Li}^+$  is:

13.73 mg/L of  $\text{Li}^+$  contains 3.59 mg/L of  $\text{Tb}^{3+}$

100 mg/L of  $\text{Li}^+$  contains  $(3.59/13.73) \times 100$  mg/L = 26.14 mg/L of  $\text{Tb}^{3+}$

So the ratio of  $\text{Li}^+ : \text{Tb}^{3+}$  present in **4a** is = 100:26.14 = 3.82:1

Or,  $\text{Tb}^{3+}$ @**4a** contains 26.14 mg Tb for each 100 mg of Li.

**Table S12.** Selective adsorption of methylene blue in different organic solvents by recent MOFs

Sl. No.	LMOF/ Coordination Polymer	Selectivity	Medium	Ref.
1.	$[(\text{CH}_3)_2\text{NH}_2][\text{In}(\text{L})]\cdot\text{CH}_3\text{CH}_2\text{OH}$ (In <sup>III</sup> -MOF)	Methylene blue	DMF	J. Mater. Chem. A 2015, 3, 14157-14164
2.	$[(\text{CH}_3)_2\text{NH}_2]_{1.5}[\text{Ln}_{1.5}(\text{TATAT})(\text{H}_2\text{O})_{4.5}]\cdot x(\text{solvent})$	Methylene blue	DMF	Inorg. Chem. 2018, 57, 11463-11473
3.	MOF1	Methylene blue	DMF	J. Mater. Chem. C 2019, 7, 8861-8867
4.	NEM-7-Zn	Methylene blue	Methanol	Inorg. Chem. Front. 2018, 5, 2898-2905
5.	$[\text{Cu}_6(\text{TATAB})_4(\text{BPY})_3]$	Methylene blue	Ethanol	Mater. Chem. Front. 2018, 2, 129-135
6.	$[(\text{CH}_3)_2\text{NH}_2][\text{Zn}_{1.5}(\mu_3\text{-O})_{0.5}(\text{F-tzba})_{1.25}(\text{bpy})_{0.25}(\mu_2\text{-F})_{0.5}]\cdot 2\text{DMF}\cdot 2\text{H}_2\text{O}$	Methylene blue	Acetonitrile	Inorg. Chem. Front. 2020, 7, 746-755
7.	$\{[(\text{CH}_3)_2\text{NH}_2]\text{In}(\text{G-1})(\text{H}_2\text{O})\}\cdot 9\text{DMF}$	Methylene blue	water	Inorg. Chem. 2019, 58, 8396-8407
8.	Fe-HAF-1	Methylene blue	water	J. Am. Chem. Soc. 2020, 142, 6907-6912
9.	CSMCRI-4	Methylene blue	DMF	This work

## References

1. *SAINT+*, version 6.02; Bruker AXS: Madison, WI, 1999.
2. G. M. Sheldrick, *SADABS*, Empirical Absorption Correction Program; University of Göttingen: Göttingen, Germany, 1997.
3. *XPREP*, version 5.1; Siemens Industrial Automation Inc.: Madison, WI, 1995.
4. G. M. Sheldrick, *SHELXTL* Reference Manual: version 5.1; Bruker AXS: Madison, WI, 1997.
5. G. M. Sheldrick, *SHELXL-2014/7*; University of Göttingen: Göttingen, Germany.
6. A. L. Spek, *PLATON*; The University of Utrecht: Utrecht, The Netherlands, 1999.
7. V. A. Blatov, *IUCr CompComm Newsletter*, 2006, **7**, 4, <http://www.topos.ssu.samara.ru>.

8. S. Nandi, D. Chakraborty and R. Vaidhyanathan, Permanently Porous Single Molecule H-Bonded Organic Framework for Selective CO<sub>2</sub> Capture, *Chem. Commun.*, 2016, **52**, 7249–7252.
9. J. Vandevondele, M. Krack, F. Mohamed, M. Parrinello, T. Chassaing and J. Hutter, Quickstep: Fast and Accurate Density Functional Calculations Using a Mixed Gaussian and Plane Waves Approach, *Comput. Phys. Commun.*, 2005, **167**, 103–128.
10. J. Vandevondele and J. Hutter, An Efficient Orbital Transformation Method for Electronic Structure Calculations, *J. Chem. Phys.*, 2003, **118**, 4365–4369.
11. G. Lippert, J. Hutter and M. Parrinello, The Gaussian and augmented-plane-wave Density Functional method for Ab Initio molecular dynamics simulations, *Theor. Chem. Acc.*, 1999, **103**, 124–140.
12. G. Lippert, M. Parrinello and J. Hutter, A hybrid Gaussian and plane wave density functional scheme, *Mol. Phys.*, 1997, **92**, 477–487.
13. J. P. Perdew, Density-functional approximation for the correlation-energy of the inhomogeneous electron-gas, *Phys. Rev. B*, 1986, **33**, 8822–8824.
14. J. P. Perdew, K. Burke and M. Ernzerhof, Generalized Gradient Approximation Made Simple. *Phys. Rev. Lett.*, 1996, **77**, 3865–3868.
15. J. Vandevondele and J. Hutter, Gaussian Basis Sets for Accurate Calculations on Molecular Systems in Gas and Condensed Phases, *J. Chem. Phys.*, 2007, **127**, 114105.
16. S. Goedecker, M. Teter and J. Hutter, Separable Dual-Space Gaussian Pseudopotentials, *Phys. Rev. B: Condens. Matter Mater. Phys.*, 1996, **54**, 1703–1710.
17. M. Krack, Pseudopotentials for H to Kr Optimized for Gradient-Corrected Exchange-Correlation Functionals, *Theor. Chem. Acc.*, 2005, **114**, 145–152.
18. S. Grimme, J. Antony, S. Ehrlich and H. Krieg, A consistent and accurate ab initio parametrization of density functional dispersion correction (DFT-D) for the 94 elements H-Pu, *J. Chem. Phys.*, 2010, **132**, 154104.
19. S. Grimme, S. Ehrlich and L. Goerigk, Effect of the damping function in dispersion corrected density functional theory, *J. Comput. Chem.*, 2011, **32**, 1456–1465.
20. J. D. H. Donnay and D. Harker, A new law of crystal morphology extending the law of Bravais, *Am. Mineral.*, 1937, **22**, 446–467.
21. G. Friedel and Etudes sur la loi de Bravais, *Bull. Soc. Fr. Mineral.*, 1907, **30**, 326–455.